





Color Dispersion as an Indicator of Stellar Population Complexity: Insights from the Pixel Color–Magnitude Diagrams of 32 Bright Galaxies in Abell 1139 and Abell 2589

Joon Hyeop Lee^{1,2} , Mina Pak^{1,2}, Hye-Ran Lee^{1,2} , and Sree Oh^{3,4,5}¹ Korea Astronomy and Space Science Institute, Daejeon 34055, Republic of Korea; jhl@kasi.re.kr² University of Science and Technology, Daejeon 34113, Republic of Korea³ Research School of Astronomy and Astrophysics, The Australian National University, Canberra, ACT 2611, Australia⁴ ARC Centre of Excellence for All Sky Astrophysics in 3 Dimensions (ASTRO 3D), Australia⁵ Department of Astronomy and Yonsei University Observatory, Yonsei University, Seoul 03722, Republic of Korea

Received 2017 November 29; revised 2018 March 14; accepted 2018 March 19; published 2018 April 20

Abstract

We investigate the properties of bright galaxies of various morphological types in Abell 1139 and Abell 2589, using pixel color–magnitude diagram (pCMD) analysis. The sample contains 32 galaxies brighter than $M_r = -21.3$ mag with spectroscopic redshifts, which are deeply imaged in the g and r bands using the MegaCam mounted on the Canada–France–Hawaii Telescope. After masking contaminants with two-step procedures, we examine how the detailed properties in the pCMDs depend on galaxy morphology and infrared color. The mean $g - r$ color as a function of surface brightness (μ_r) in the pCMD of a galaxy shows good performance in distinguishing between early- and late-type galaxies, but it is not perfect because of the similarity between elliptical galaxies and bulge-dominated spiral galaxies. On the other hand, the $g - r$ color dispersion as a function of μ_r works better. We find that the best set of parameters for galaxy classification is a combination of the minimum color dispersion at $\mu_r \leq 21.2$ mag arcsec⁻² and the maximum color dispersion at $20.0 \leq \mu_r \leq 21.0$ mag arcsec⁻²; the latter reflects the complexity of stellar populations at the disk component in a typical spiral galaxy. Finally, the color dispersion measurements of an elliptical galaxy appear to be correlated with the *Wide-field Infrared Survey Explorer* infrared color ([4.6]–[12]). This indicates that the complexity of stellar populations in an elliptical galaxy is related to its recent star formation activities. From this observational evidence, we infer that gas-rich minor mergers or gas interactions may have usually occurred during the recent growth of massive elliptical galaxies.

Key words: galaxies: clusters: individual (Abell 1139, Abell 2589) – galaxies: elliptical and lenticular, cD – galaxies: evolution – galaxies: formation – galaxies: spiral

1. Introduction

A comprehensive understanding of the formation histories of galaxies with a variety of morphologies is a major goal in modern astronomy. Beyond the classical paradigms about the formation of massive galaxies such as the monolithic collapse model (Patridge & Peebles 1967; Tinsley 1972; Larson 1974) and the hierarchical merging model (Toomre 1977; Searle & Zinn 1978), a huge number of studies in recent decades have illuminated various aspects of the mass assembly and star formation histories of galaxies. Currently, much observational evidence supports a galaxy formation scenario that is more complicated than was classically assumed: massive galaxies may have formed through two-phase and inside-out formation processes (e.g., Oser et al. 2010; van Dokkum et al. 2010; Lee & Yi 2013; Pastrello et al. 2015; Liu et al. 2016). In this scenario, massive galaxies have experienced violent starburst and subsequent star formation quenching at a relatively early epoch, which partially resembles the classical monolithic collapse. On the other hand, such a violent starburst is thought to be often triggered by gas-rich major mergers, and those galaxies are found to have kept growing via numerous minor mergers for a long time after the early starburst and quenching, which is consistent with the hierarchical build-up scheme.

Although recent observational and theoretical achievements shed light on our understanding of galaxy formation by suggesting a reasonable solution to the apparent contradiction between the classical models, several detailed issues are still obscured. For example, it is not completely understood how the recent histories of star formation and mass assembly in massive

galaxies are related to each other. Several recent studies have argued that the major formation process of early-type galaxies depends on their masses, in the context that low-mass, early-type galaxies tend to have experienced gas-rich mergers, whereas massive early-type galaxies have grown via dry mergers (Kormendy et al. 2009; Bernardi et al. 2011; Lee et al. 2013). However, whereas those findings well explain the average trends of galaxy formation, we encounter various exceptions such as massive galaxies with evidence of recent star formation activity (e.g., Lee et al. 2006; Fernández-Ontiveros et al. 2011; George 2017; Sheen et al. 2017).

It is relatively easy to trace current or recent star formation in a galaxy using various well-defined indicators, such as optical or ultraviolet–optical colors, spectral emission lines, and infrared or radio luminosity. On the other hand, the method to trace recent mass assembly events is not very well established, compared to star formation measurement. One may determine whether a galaxy recently experienced merging events, or not, by decomposing its internal structure and estimating its structural asymmetry or irregularity. However, such an approach requires much effort for each galaxy, and quantitative comparison between different galaxies is not easy. Thus, if a simple and efficient indicator of recent mass assembly could be devised, it would be very useful for investigating recent evolution histories of a large number of galaxies, in combination with the tracers of recent star formation activity.

A candidate for such a simple and efficient methodology to trace the formation history of a galaxy is pixel color–magnitude

diagram (pCMD) analysis (Bothun 1986; Abraham et al. 1999; de Grijs et al. 2003; Lanyon-Foster et al. 2007; Lee et al. 2011, 2012, 2017). This method has not been very widely used to date, but it has the potential to be a powerful approach toward a total understanding of the photometric and structural properties of galaxies. For example, Lanyon-Foster et al. (2007) showed that galaxies of various morphological types show varied and distinct features in their pCMDs, such as *prime sequences* for early-type galaxies and *inverse-L* features for spiral galaxies. Compared to the classical photometric and/or structural analysis methods, pCMD analysis has several advantages: (1) it can be consistently applied to galaxies with any kind of morphology, (2) it considers the photometric and structural properties at the same time, and (3) it is efficient in checking the homology between galaxies at different mass or size scales (Lee et al. 2017).

Despite such merits, however, usage of the pCMD analysis is not yet completely established. As an effort to devise a quantitative analysis method using this technique, Lee et al. (2017) introduced simple routines to compare pCMDs to check similarities in galaxy formation history. They compared the brightest cluster galaxies (BCGs) in Abell 1139 (A1139) and Abell 2589 (A2589), which are two of the 14 galaxy clusters targeted in the KASI–Yonsei Deep Imaging Survey of Clusters (KYDISC; Oh et al. 2018). By simplifying the overall pCMD features into the mean and standard deviation of pixel color as a function of pixel surface brightness (called a pCMD *backbone*), Lee et al. (2017) showed that the BCG of the dynamically relaxed A2589 formed a larger central body at an early epoch and has grown to be a larger, more massive, and dynamically better relaxed galaxy today than the BCG of the dynamically young A1139. These results support the idea that a BCG and its host cluster coevolve.

As shown in Lee et al. (2017), pCMD backbone analysis is a useful method for comparing the formation histories of galaxies even with different mass or size scales, but it needs to be simplified further to be efficiently applied to a large number of galaxies. One of its relevant parameters is the color dispersion at given μ_r in a pCMD. This quantity is thought to reflect the complexity of stellar populations. That is, a dynamically young galaxy, in which multiple stellar populations are not well mixed spatially, must have large color dispersion. Based on this inference, Lee et al. concluded that the BCG of A1139 is dynamically younger than that of A2589. However, since BCGs usually have simple structures, it will be worth examining the performance of this parameter for more varied galaxies.

This is the second in a series of papers presenting pCMD analysis results of the KYDISC cluster galaxies. In this paper, we present our pCMD study of 32 bright galaxies in A1139 and A2589. The goals of this paper are (1) to examine how the pCMD properties depend on galaxy morphology quantitatively, and (2) to understand how the stellar population complexity of a galaxy indicated by color dispersion in a pCMD is related to recent star formation activity represented by infrared color. This paper is outlined as follows. Section 2 describes the observations and sample selection. Section 3 presents the standard and alternative procedures for masking contaminants to yield final pCMDs. The results of the pCMD properties depending on morphology and star formation activity are shown in Section 4. The implication of our results is discussed in Section 5, and finally the conclusions are drawn in

Section 6. In Appendix A, additional figures showing the detailed processes of masking contaminants are presented. The final results after the alternative masking procedure are shown in Appendix B, which are in good agreement with the results after the standard masking procedure. Throughout this paper, we adopt the cosmological parameters: $h = 0.7$, $\Omega_\Lambda = 0.7$, and $\Omega_M = 0.3$.

2. Observations and Targets

2.1. Canada–France–Hawaii Telescope Observations and Sample Selection

Our data set was obtained using the MegaCam mounted on the 3.6 m Canada–France–Hawaii Telescope in 2012–2013, as a part of the KYDISC project. Among the 14 nearby clusters at $0.016 \leq z \leq 0.145$ observed in the KYDISC project, the target clusters in this paper are A1139 and A2589, which are at very similar low redshifts ($z \sim 0.04$). This similarity in redshift makes the pCMD comparison much easier, because the galaxies in the two target clusters have almost the same conversion factors from angular size to physical scale (~ 0.8 kpc arcsec $^{-1}$) and central wavelengths at the rest frame. See Table 1 of Lee et al. (2017) for the basic information on the two target clusters.

In the g and r bands, each cluster was deeply imaged with total exposure time of 2940 s. After pre-processing and image stacking, the final resampled pixel scale was $0''.185$ and the stellar full width at half maximum was about $0''.8$. Based on the redshift information retrieved from the Sloan Digital Sky Survey (York et al. 2000), NASA Extragalactic Database,⁶ and SIMBAD Astronomical Database,⁷ cluster members were selected using the difference in recession velocity from the host cluster ($|\Delta v_{\text{rec}}| \leq 3\sigma_{\text{cl}}$) and the clustercentric distance ($R \leq 2R_{200}$), where σ_{cl} and R_{200} are the velocity dispersion and virial radius of a given cluster, respectively. More details about the KYDISC project and its data products are described in Oh et al. (2018).

In this paper, we investigate the bright ($M_r \leq -21.3$ mag) galaxies in A1139 and A2589 using pCMD analysis. Among the selected cluster members, there are 16 and 15 galaxies brighter than the magnitude cut in A1139 and A2589, respectively. In addition to these 31 member galaxies, there is a bright galaxy (A1139-00004) that satisfies $|\Delta v_{\text{rec}}| \leq 3\sigma_{\text{cl}}$ but is located at $2.2 \times R_{200}$ distance from the A1139 center. This galaxy is not a member of A1139 in our selection criteria, but we include it in our sample. Since this paper is not focused on environmental effects, the important fact is that this galaxy is at a distance from us similar to those of the cluster members, not its actual membership.

In this paper, we do not apply k -correction to either pixel surface brightness or total magnitude, because the k -correction based on two-band color may not be sufficiently reliable, particularly when the photometric uncertainty is large (e.g., faint pixels). Lee et al. (2017) did not apply k -correction to pixel surface brightness either, but they applied it to total magnitude when selecting cluster members for comparison with BCGs. Thus, the sample in this paper does not exactly coincide with the comparison sample in Lee et al. (2017). Despite this difference, we decided that the photometric

⁶ <http://ned.ipac.caltech.edu>

⁷ <http://simbad.u-strasbg.fr/simbad/>

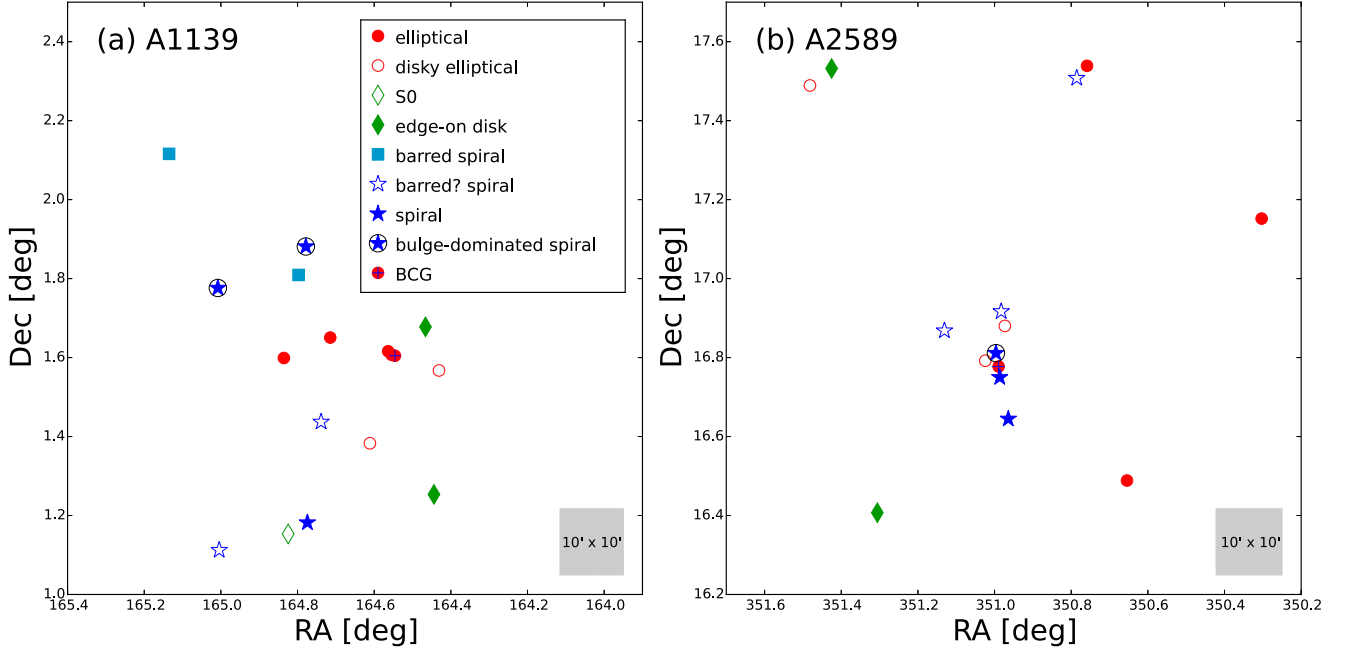


Figure 1. Spatial distribution of the sample galaxies in (a) A1139 and (b) A2589. The visually classified morphological types are denoted (see Section 2.2 for the details). The gray box in each panel shows an angular scale of $10' \times 10'$ ($\approx 0.5 \times 0.5 \text{ Mpc}^2$).

Table 1
Basic Information on the Sample Galaxies

Name	R.A. (hh:mm:ss)	Decl. (dd:mm:ss)	Redshift	M_r (mag)	$g - r$ (mag)	$ \Delta v_{\text{rec}} /\sigma_{\text{cl}}$	R/R_{200}	B/T	Morphology
A1139-00001	10:58:11.0	+01:36:17	0.038	-22.801	0.842	0.88	0.27	0.94	elliptical (BCG)
A1139-00002	10:59:17.9	+01:09:12	0.039	-22.202	0.756	0.21	1.15	0.61	S0
A1139-00003	10:58:51.5	+01:39:02	0.040	-22.187	0.803	0.04	0.62	0.82	elliptical
A1139-00004	11:00:32.4	+02:06:57	0.039	-22.165	0.675	0.26	2.17	0.21	barred spiral
A1139-00005	10:58:26.7	+01:22:59	0.041	-22.151	0.823	0.69	0.37	0.70	disky elliptical
A1139-00006	10:58:57.2	+01:26:13	0.041	-22.083	0.695	1.12	0.57	0.26	barred? spiral
A1139-00007	10:59:20.5	+01:35:56	0.039	-22.059	0.826	0.48	0.83	0.69	elliptical
A1139-00008	11:00:01.9	+01:46:34	0.040	-22.039	0.841	0.30	1.40	0.42	spiral (bulge-dominated)
A1139-00009	10:59:06.8	+01:52:52	0.041	-21.934	0.759	0.56	1.15	0.65	spiral (bulge-dominated)
A1139-00010	10:58:15.2	+01:36:58	0.039	-21.841	0.828	0.32	0.31	0.58	elliptical
A1139-00011	10:57:51.9	+01:40:40	0.041	-21.808	0.809	1.04	0.46	0.44	edge-on disk
A1139-00012	10:58:13.0	+01:36:25	0.039	-21.807	0.818	0.85	0.28	0.64	elliptical
A1139-00013	10:57:46.6	+01:15:13	0.039	-21.778	0.817	0.41	0.64	0.87	edge-on disk
A1139-00014	10:57:43.4	+01:34:02	0.039	-21.705	0.808	0.41	0.28	0.77	disky elliptical
A1139-00015	10:59:05.8	+01:10:55	0.039	-21.693	0.540	0.57	1.02	0.03	spiral
A1139-00016	10:59:11.4	+01:48:33	0.040	-21.442	0.655	0.10	1.04	0.44	barred spiral
A1139-00017	11:00:01.1	+01:06:44	0.039	-21.334	0.709	0.59	1.55	0.09	barred? spiral
A2589-00001	23:23:57.5	+16:46:38	0.041	-23.807	0.838	0.09	0.04	0.98	elliptical (BCG)
A2589-00002	23:25:42.0	+17:31:55	0.041	-22.000	0.849	0.06	1.04	0.44	edge-on disk
A2589-00003	23:23:08.5	+17:30:28	0.038	-21.970	0.572	1.12	0.89	0.17	barred? spiral
A2589-00004	23:24:31.4	+16:52:05	0.036	-21.907	0.482	1.89	0.20	0.39	barred? spiral
A2589-00005	23:23:51.4	+16:38:41	0.035	-21.747	0.448	2.20	0.20	0.09	spiral
A2589-00006	23:22:37.1	+16:29:19	0.037	-21.706	0.818	1.36	0.55	0.72	elliptical
A2589-00007	23:23:59.1	+16:48:40	0.043	-21.654	0.863	0.39	0.03	0.91	spiral (bulge-dominated)
A2589-00008	23:23:53.5	+16:52:48	0.045	-21.653	0.875	1.17	0.09	0.30	disky elliptical
A2589-00010	23:23:56.8	+16:44:60	0.038	-21.500	0.837	1.01	0.07	0.68	elliptical
A2589-00011	23:25:55.6	+17:29:21	0.046	-21.466	0.591	1.55	1.03	0.03	spiral
A2589-00012	23:25:13.4	+16:24:26	0.039	-21.427	0.856	0.78	0.63	0.40	disky elliptical
A2589-00013	23:24:05.8	+16:47:31	0.042	-21.426	0.879	0.09	0.06	0.73	edge-on disk
A2589-00014	23:23:55.8	+16:55:00	0.041	-21.390	0.853	0.06	0.13	0.62	disky elliptical
A2589-00015	23:23:02.1	+17:32:20	0.038	-21.381	0.775	1.24	0.93	0.69	barred? spiral
A2589-00018	23:23:54.4	+16:40:50	0.045	-21.321	0.828	1.24	0.16	0.68	elliptical

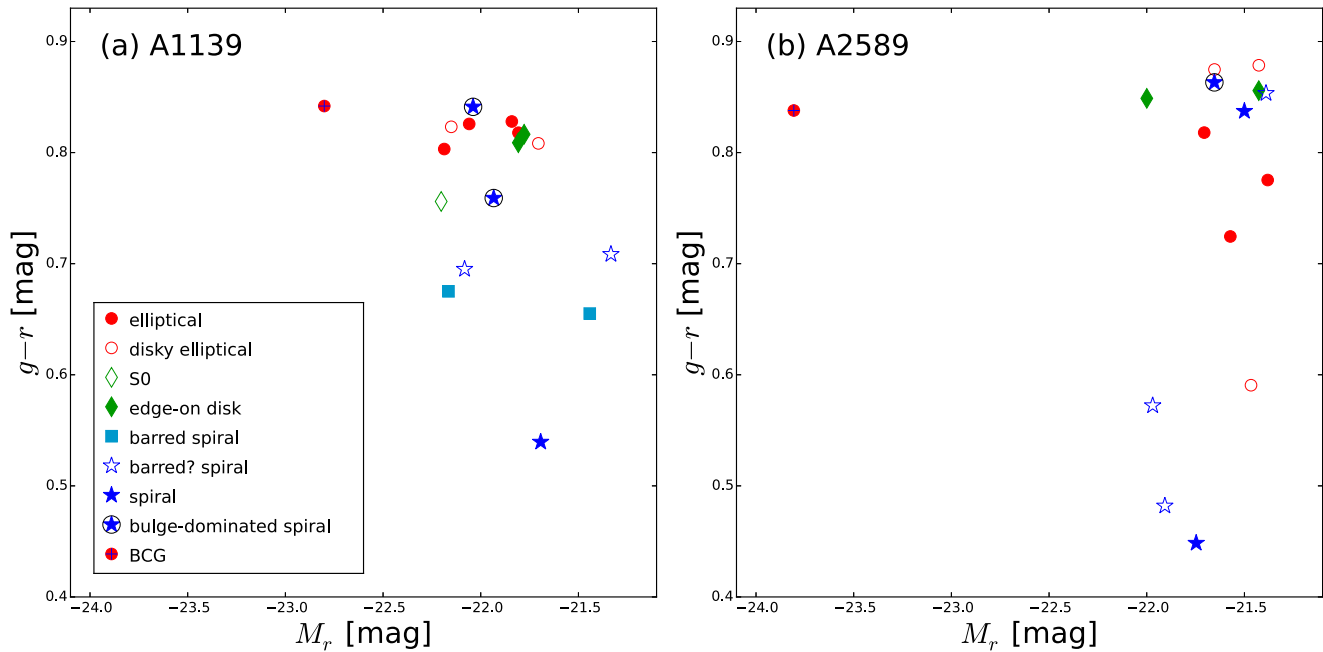


Figure 2. Total color–magnitude diagrams of the sample galaxies in (a) A1139 and (b) A2589, with the morphological types denoted.

consistency between the pixel and total magnitudes is more important in this paper.

The basic information on our sample galaxies is summarized in Table 1. The right ascensions (R.A.) and declinations (decl.) are for the J2000 epoch. All magnitudes and surface brightness in this paper were corrected for Galactic extinction using the method of Schlafly & Finkbeiner (2011), in the AB magnitude system. Figure 1 presents the spatial distribution of the selected sample galaxies, while their total CMDs are shown in Figure 2. The r -band portrait images of our sample galaxies are displayed in Figure 3.

2.2. Morphological Classification

Figure 4 shows the r -band surface brightness (μ_r) maps, which reveal the internal structures of our sample galaxies more clearly. Based on Figures 3 and 4, authors J.H.L., M.P., and H.R.L. visually classified the morphological types of our sample galaxies into the following classes:

1. typical elliptical (E): well-defined elliptical structures without any disturbed features,
2. disk elliptical (disky E): overall elliptical morphology with slightly disk-like internal structures (but not significantly different from typical elliptical galaxies),
3. lenticular (S0): hosting a faint disk component and not significantly inclined (face-on),
4. edge-on disk: largely inclined S0 or late-type (but mostly bulge-dominated in our sample),
5. barred spiral: spiral arms connected to a bar structure (a question mark is denoted when the bar is ambiguous), and
6. spiral: spiral arms without a bar structure.

Since the bulge fraction affects the overall properties of a late-type galaxy, a mark of “BD” is additionally noted for a bulge-dominated, late-type galaxy. The morphological classification is sometimes ambiguous: E versus disk E, disk E versus S0, and S0 versus bulge-dominated spiral. However, the small

ambiguity between some types does not significantly matter here, because we are mainly focused on the difference between broadly divided early- and late-type galaxies rather than between individual fine classes. Note that the classification in this paper was conducted independently of that in the KYDISC catalog, and thus they may not necessarily coincide with each other. For example, A1139-00008 is listed as an S0 galaxy in the KYDISC catalog, but we classify it as a bulge-dominated spiral, because of very faint ambient features around it. As a quantitative indicator of morphology, we also estimated the bulge-to-total ratio (B/T) of each galaxy, based on the decomposition into Sérsic component (bulge) + exponential component (disk) using the GALFIT code (Peng et al. 2002, 2010).

Figure 5 presents the $g-r$ color maps of our sample galaxies. The internal distributions of stellar populations are revealed in these maps, which are particularly useful in visually inspecting the interactions with neighbor galaxies (e.g., A1139-00009 and A1139-00017). Note that our morphological classification is not based on these color maps, but only on the light distributions in the r band.

2.3. WISE Data

Infrared color is a useful tool to diagnose star formation and nucleus activities of galaxies (Assef et al. 2010; Jarrett et al. 2011, 2017; Ko et al. 2016). In this paper, we use *Wide-field Infrared Survey Explorer* (WISE; Wright et al. 2010) data. WISE mapped the whole sky in four infrared bands: 3.4, 4.6, 12, and 22 μm ($W1$, $W2$, $W3$, and $W4$) with angular resolutions of $6''1$, $6''4$, $6''5$, and $12''0$, respectively.

From the WISE website,⁸ we retrieved infrared magnitudes for our target galaxies. For most point-like sources in the WISE data, the recommended magnitude type is the *profile-fit magnitude*, but we use the *elliptical aperture magnitude* instead, because our targets are mostly extended sources even

⁸ <http://wise2.ipac.caltech.edu/docs/release/allsky/>

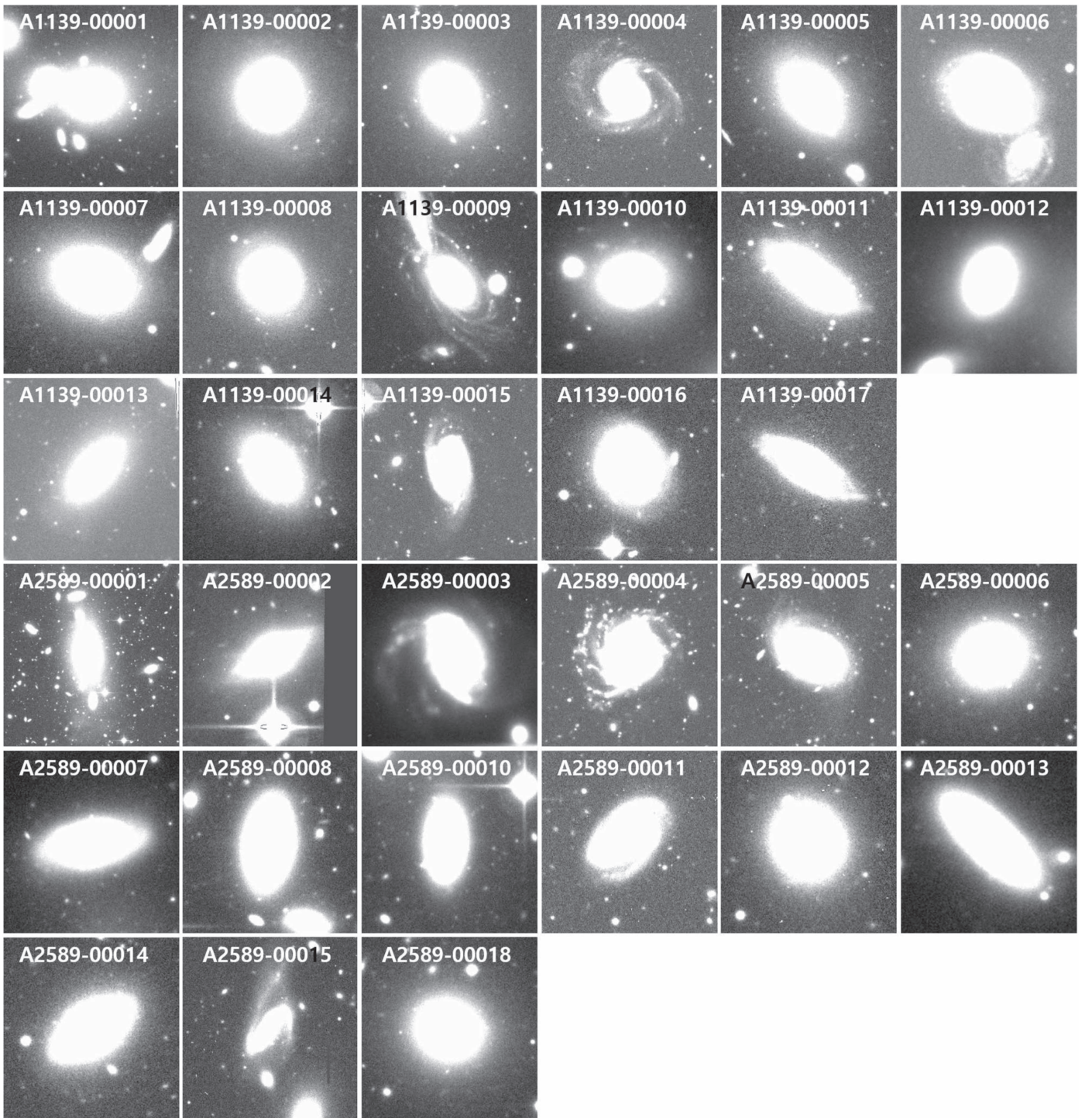


Figure 3. Portrait images of the sample galaxies in the r band. Denoted at the top of each panel is the identity number in the KYDISC catalog.

in the *WISE* images. The elliptical apertures in the *WISE* photometry are based on cross-matching with the Two Micron All Sky Survey Extended Source Catalog (2MASS XSC; Skrutskie et al. 2006). However, the aperture magnitude is not available for one of our targets (A2589-00014), which means that this object looks like a point source in the infrared images although it is an extended source at higher resolution. Thus, we use the profile-fit magnitude only for A2589-00014.

We adopt the $[4.6]-[12]$ ($W2 - W3$) color as a star formation indicator, because the $[12]$ band flux is sensitive to star formation activity whereas the $[4.6]$ band flux reflects age-

independent stellar mass. On the other hand, the $[3.4]-[4.6]$ ($W1 - W2$) color is known to be an indicator of active galactic nuclei (AGNs), owing to its sensitivity to hot dust (Jarrett et al. 2017). These color indices are used to describe the star formation properties of the sample galaxies.

3. Analysis

3.1. Standard Procedure for Masking Contaminants

Before plotting final pCMDs, target images need to be appropriately processed to minimize the influence of contaminants

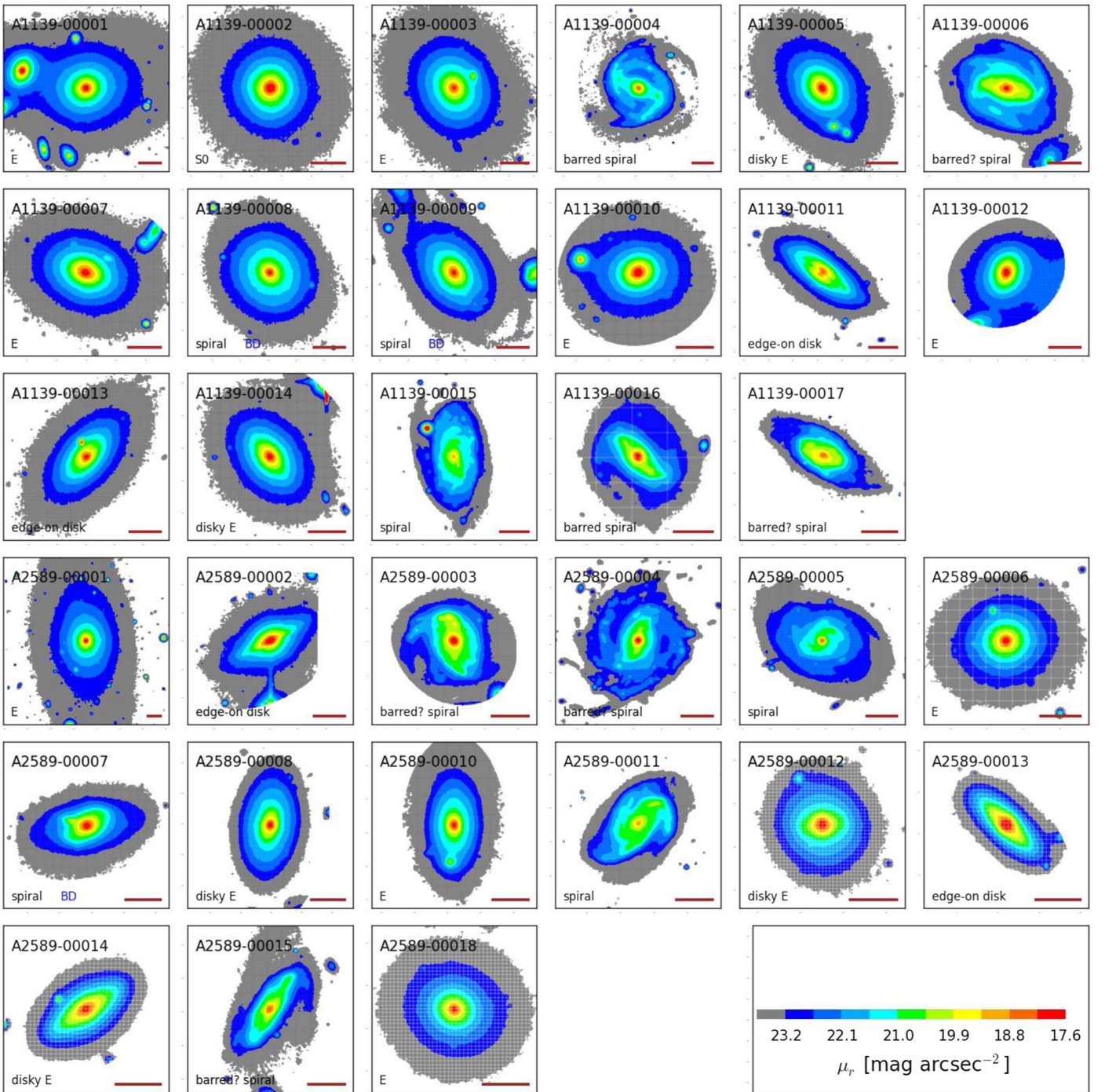


Figure 4. r -band surface brightness maps of the sample galaxies. Visually classified morphology is denoted in the lower left corner and the 10 arcsec (~ 8 kpc) scale bar is shown in the lower right corner of each panel. See the main text for a detailed description of each morphological type.

and to improve the signal-to-noise ratio (S/N) of each pixel. Lee et al. (2017) established a procedure for the pCMD analysis, which includes contaminant-masking and pixel-smoothing. The procedure is summarized as follows.

1. Trim a sufficient area around a target galaxy.
2. Detect objects using the Source Extractor (SE; Bertin & Arnouts 1996) with sufficiently large background mesh sizes (to detect relatively large contaminants).
3. Use the SE again with small background mesh sizes (to detect small and faint contaminants).

4. Mask the pixels within the apertures of any detected non-target objects.
5. Smooth pixels by adopting a smoothing kernel with a seeing-sized ($0''.08$) aperture.

In Lee et al. (2017), this procedure worked well, because the target galaxies were BCGs with relatively simple shapes and few complex substructures.

In this paper, on the other hand, the targets are galaxies of various morphologies, from elliptical to spiral. Because elliptical galaxies (and most edge-on disk galaxies) do not

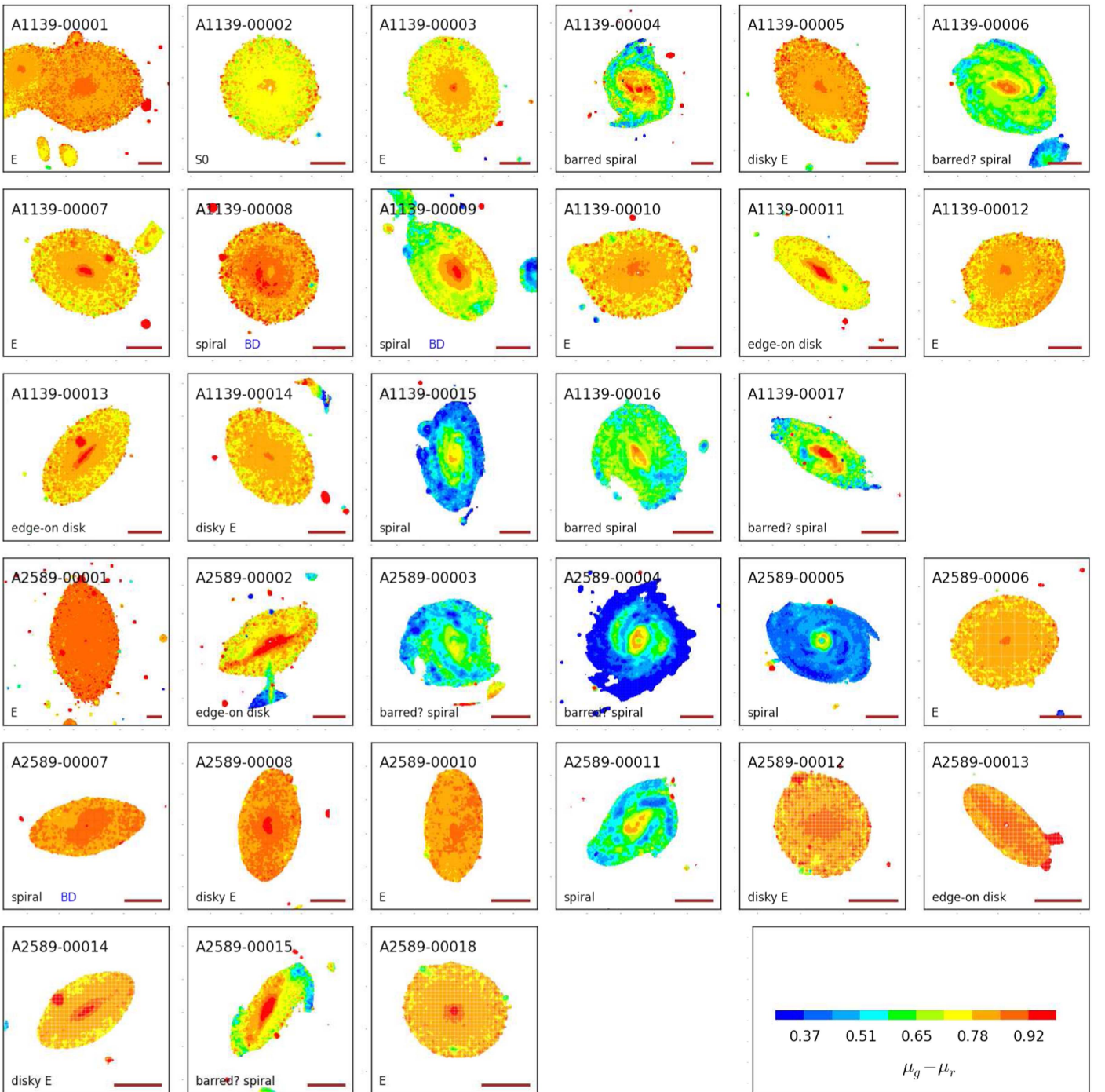


Figure 5. $g - r$ color maps of the sample galaxies. Pixels fainter than $\mu_r = 23.2 \text{ mag arcsec}^{-2}$ are not plotted. The visually classified morphology and the 10 arcsec scale bar are also denoted.

show complex structures in their r -band images, there is no problem in applying SE-detection-based masking to them. In the case of late-type galaxies, however, this does not work well, because the SE hardly distinguishes between contaminants (companions or foreground/background objects) and galaxy substructures (spiral arms, star-forming clumps, and bars). For a few late-type galaxies, SE-detection-based masking removes more than 80% of the entire image for a target galaxy, which is obviously over-masking.

Thus, we apply SE-detection-based masking adaptively according to the target morphology and the masking performance.

That is, the full procedure is applied if SE-detection-based masking does not cause over-masking (e.g., A1139-00003). On the other hand, if this method (step 2 and/or step 3 in the procedure) appears to over-mask the target galaxy, the masking step is omitted (e.g., A1139-00004). During this adaptation, we intended to minimize the omission of masking. That is, the masking step is omitted only when it obviously over-masks the target galaxy, whereas it is conducted when it is unclear whether the target is over-masked or not. Among our sample galaxies, there was rarely an ambiguous situation and thus we decided the final masking sets relatively easily.

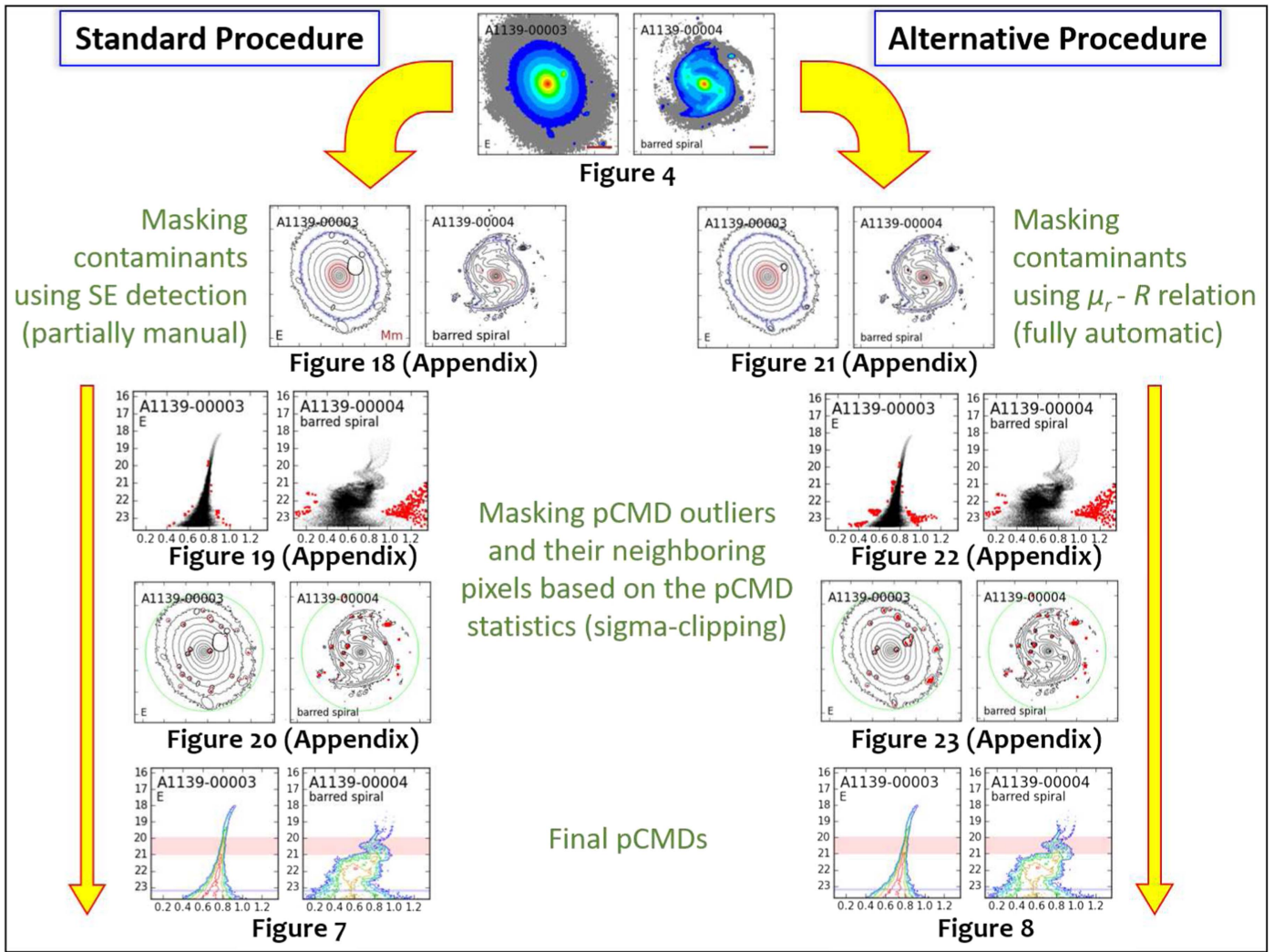


Figure 6. Schematic summary of the standard and alternative procedures. The left-side sequence shows the standard procedure (described in Section 3.1), while the right-side sequence shows the alternative procedure (described in Section 3.2). The full plots for the whole sample of galaxies in each masking process are presented in Appendix A.

However, adaptive masking has a fundamental weakness: late-type galaxies with complicated structures tend to be masked too little, compared to early-type galaxies with simple structures. Because late-type galaxies are expected to have remaining contaminants that were not sufficiently masked in the SE-detection-based masking process, a supplementary process is necessary. For this, we additionally masked the pixels that correspond to the pCMD outliers. The processes are listed as follows.

1. Estimate the 5, 50, and 95 percentiles in the pixel $g - r$ color distribution at given μ_r , using the pCMD after the SE-detection-based masking.
2. Define $\sigma_1 \equiv (g - r)_{50\%} - (g - r)_{5\%}$ and $\sigma_2 \equiv (g - r)_{95\%} - (g - r)_{50\%}$ as a function of μ_r .
3. Define pCMD outliers as the pixels with $g - r < (g - r)_{50\%} - 2\sigma_1$ or $g - r > (g - r)_{50\%} + 2\sigma_2$, at given μ_r .
4. Mask the pCMD outliers and their neighboring pixels within $0''.8$ (seeing size).

Figure 6 schematically summarizes the entire masking procedure to yield the final pCMDs (the standard procedure

on the left). The plots in the second row of the left side in Figure 6 show the surface brightness contour maps of the sample galaxies after the adaptive (SE-detection-based) masking. The plots in the third row of the left side show the pCMDs after SE-detection-based masking and smoothing with the $0''.8$ -aperture spline kernel (Lee et al. 2017), with the pCMD outliers marked (see Appendix A for the full plots of the whole sample). The pCMD outliers of late-type galaxies mostly outnumber those of early-type galaxies, which means that many remaining contaminants in late-type galaxies are additionally masked in this process.

Note that the pCMD outlier masking is not perfect either. There may still be remaining contaminants or there may be some over-masking, particularly for fine substructures in the target galaxies. For example, the BCG of A2589 (A2589-00001) is thought to have vestiges of infalling low-mass, star-forming satellites, which was revealed from the analysis of its pCMD outliers in Lee et al. (2017). Such fine features are mostly washed out in the pCMD outlier masking process. Thus, this process cannot be used if we want to inspect the fine substructures in target galaxies. However, it does not significantly affect the main features of the pCMD backbones,

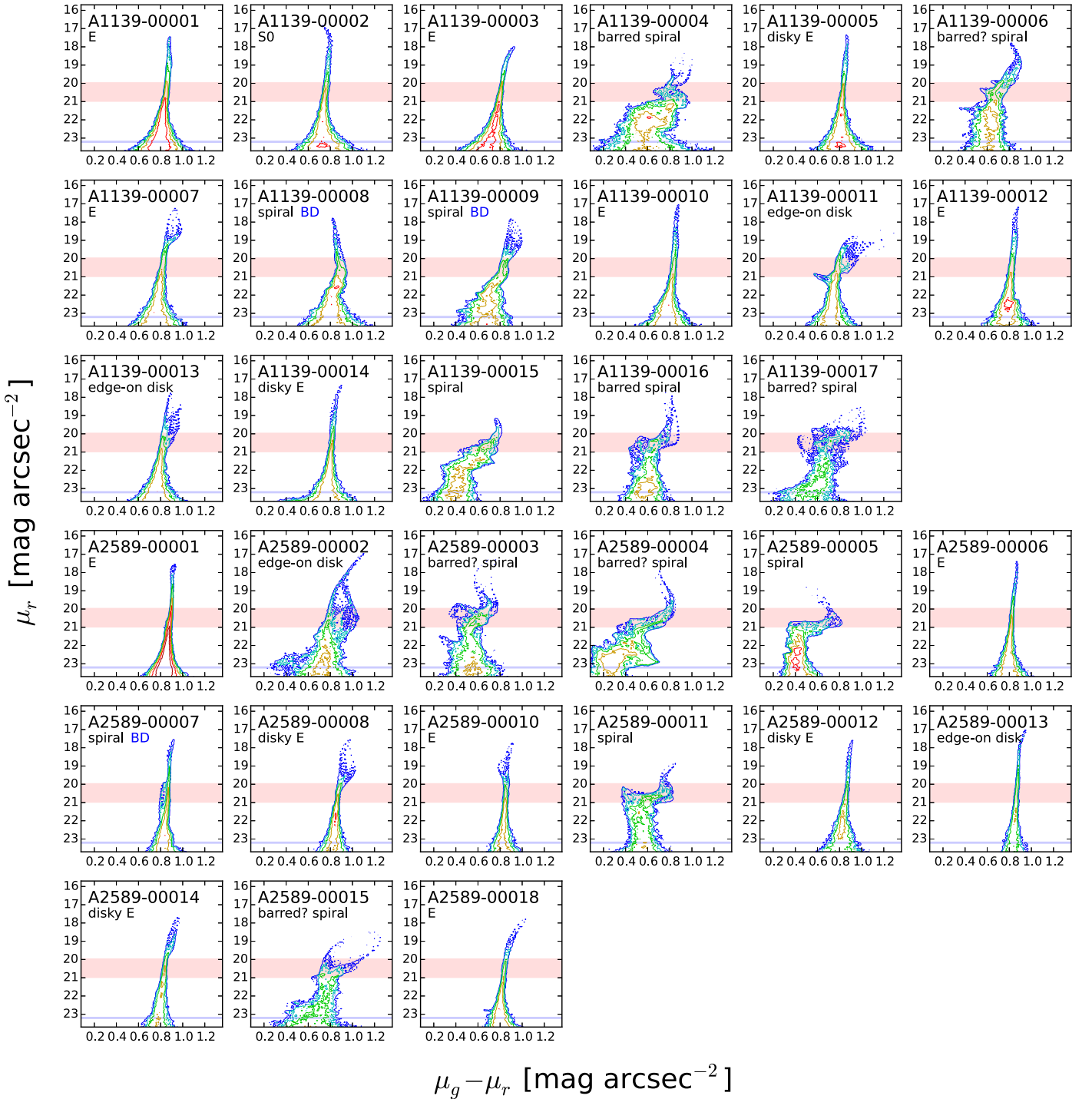


Figure 7. Log-scale pixel number density contours of the final pCMDs after the standard masking procedure. The $20.0 \leq \mu_r \leq 21.0$ mag arcsec $^{-2}$ range (faint red stripe) and the $\mu_r = 23.2$ mag arcsec $^{-2}$ limit (faint blue line) are denoted.

because the number of outliers is typically much smaller than that of the pixels in the main features. The plots in the fourth row in Figure 6 present the μ_r contour maps after masking the pCMD outliers and their neighboring pixels within $0''.8$. After this two-step masking process, the final pCMDs are yielded as shown in Figure 7.

3.2. Alternative Procedure

In the standard procedure, the SE-detection-based masking process for contaminants has two weaknesses. One is that

late-type galaxies cannot be sufficiently masked using this method, which is ameliorated to some extent by using the pCMD outlier masking as described in Section 3.1. However, another weakness remains: “adaptive masking” can cause a bias when we compare the pCMD properties between different morphological types. As already mentioned, late-type galaxies tend to be less suitable for SE-detection-based masking than early-type galaxies. Among the 13 spiral galaxies, SE-detection-based masking was completely omitted for four spirals (A1139-00004, A2589-00003, A2589-00004, and A2589-00011), while

full masking was applied to only two spirals (A1139-00008 and A2589-00007). On the other hand, full masking was applied to every elliptical galaxy. That is, the masking processes for early- and late-type galaxies are not identical in the standard procedure, and thus a comparison of the final pCMDs between galaxies with different morphological types may not be appropriate.

To address this issue, we try an alternative masking procedure that does not depend on subjective ‘‘adaptation’’ according to galaxy morphology. This procedure is based on the idea that the light from contaminants tends to be brighter than the brightness expected at the distance from the target galaxy center. The detailed procedure is as follows.

1. Trim a sufficient area around a target galaxy.
2. Trim the image again with a radius of $f_c \times R80_{(22.2-23.2)}$, where f_c is a fixed value and $R80_{(22.2-23.2)}$ is the 80 percentile in the distribution of distance to center, among pixels with $22.2 \leq \mu_r \leq 23.2$ mag arcsec⁻²; we empirically choose $f_c = 1.5$ (see Appendix A for the trimming area for each sample galaxy).
3. Estimate the 10 and 50 percentiles in the distribution of distance to center, among pixels with given μ_r ($R10_{\mu_r}$ and $R50_{\mu_r}$, respectively).
4. Mask pixels with μ_r and radial distance (R) satisfying $R - R10_{\mu_r} > f_R \times (R50_{\mu_r} - R10_{\mu_r})$, where we empirically choose $f_R = 5$.
5. Conduct the additional pCMD outlier masking as described in Section 3.1.

These processes depend on a few control parameters being empirically determined, which is a weakness. Nevertheless, this method has the considerable merit that it can be consistently applied to target galaxies regardless of their morphological type.

The plots in the second row of the right side in Figure 6 show the surface brightness contour maps after this μ_r -radius-relation-based ($R(\mu_r)$ -based) masking. The overall area masked by the $R(\mu_r)$ -based method tends to be smaller (under-masking) than that by the SE-detection-based method. Thus, the role of the pCMD outlier masking is more important in the alternative procedure, because it augments the weak performance of the $R(\mu_r)$ -based masking. In this procedure, the number of pCMD outliers is, on average, not so different between early- and late-type galaxies, unlike in the standard procedure. This is because the alternative masking procedure is free from the morphology bias caused by subjective ‘‘adaptation.’’

The final pCMDs after alternative masking are presented as pixel number density contours in Figure 8. The overall features of the pCMDs in Figure 8 are not significantly different from those after standard masking in Figure 7, but some small details appear to differ. Such differences are revealed in Figure 9, which shows the pixel number density contours for the pCMD residuals (Figure 7 subtracted by Figure 8). In most cases, the pixels in the pCMDs after the alternative procedure outnumber those after the standard procedure (blue contours). This means that the alternative procedure is less efficient in masking contaminants than the standard procedure, at least for early-type galaxies. The opposite case is much rarer (red contours) even for late-type galaxies. It is hard to increase the masking efficiency of the alternative procedure by adjusting f_R , because a too small f_R value frequently results in unreasonable masking.

In summary, the alternative procedure is not sufficient in the aspect of masking efficiency, but the results from it are necessary when a technically fair comparison without any morphology bias

is required. In Section 4, we mainly analyze the results from the standard procedure, to take advantage of its masking efficiency (mainly for early-type galaxies). However, the results from the alternative procedure are also used to check the effect of morphology bias, and these are fully presented in Appendix B.

4. Results

4.1. Overall Description of the pCMDs

In the final pCMDs (Figures 7 and 8), early-type galaxies show simple pCMD features, whereas late-type galaxies show significantly curved pCMDs. As introduced in Section 1, those features are called prime sequences and inverse-L features in Lanyon-Foster et al. (2007), respectively. However, such a dichotomic division is not always obvious. Some early-type galaxies have considerably disturbed features at their bright parts (A1139-00007, A2589-00008, and A2589-00014) and, besides, the pCMDs of some bulge-dominated late-type galaxies or edge-on disk galaxies are similar to those of early-type galaxies (A2589-00007 and A2589-00013). That is, galaxies even of similar morphological types have some variety in their pCMD features, and this variety is broader in late-type galaxies.

In early-type galaxies, the unusual features (deviations from the prime sequences) seem to be closely related to tidal interactions with nearby neighbors or companions. The prime sequences of the elliptical galaxies show curvatures different from one another, which implies that their formation histories are not entirely homologous, as discussed in Lee et al. (2017). Different internal dust extinction may also be responsible for such variety (Lee et al. 2011, 2012). The only face-on S0 galaxy in our sample (A1139-00002) shows a blue pCMD-tip feature, which indicates that this galaxy may have experienced central star formation activity very recently.

The (barred and unbarred) spiral galaxies show complex and diverse features in their pCMDs. The pCMD structure of a spiral galaxy is roughly described as consisting of a (red and bright) bulge part and a (blue and faint) disk part, which form an overall inverse-L feature. However, whereas this division is quite clear in some spiral galaxies (A1139-00016, A2589-00004, and A2589-00011), some others show more complicated and amorphous features (A1139-00017 and A2589-00015). The bulge-dominated spiral galaxies (A1139-00008, A1139-00009, and A2589-00007) show relatively simple pCMD features compared to the other spiral galaxies, but these are more distorted than the pCMDs of typical elliptical galaxies.

Finally, some edge-on disk galaxies (A1139-00013 and A2589-00013) have pCMDs similar to those of elliptical galaxies, but some others do not (A1139-00011 and A2589-00002). The former appear quite elliptical in their r -band images (Figure 3), but they were classified into edge-on disks because an edge-on dust lane was found (A1139-0013) or the morphology was too elongated to be an elliptical galaxy (A2589-00013). The latter are clearly different from elliptical galaxies in their appearance.

4.2. Quantitative Comparison

One of the main purposes of this paper is to establish a quantitative method using pCMDs to distinguish between galaxies with different morphological types. For a quantitative comparison of the pCMD features, we devised several parameters describing the features of pCMDs as listed in Table 2.

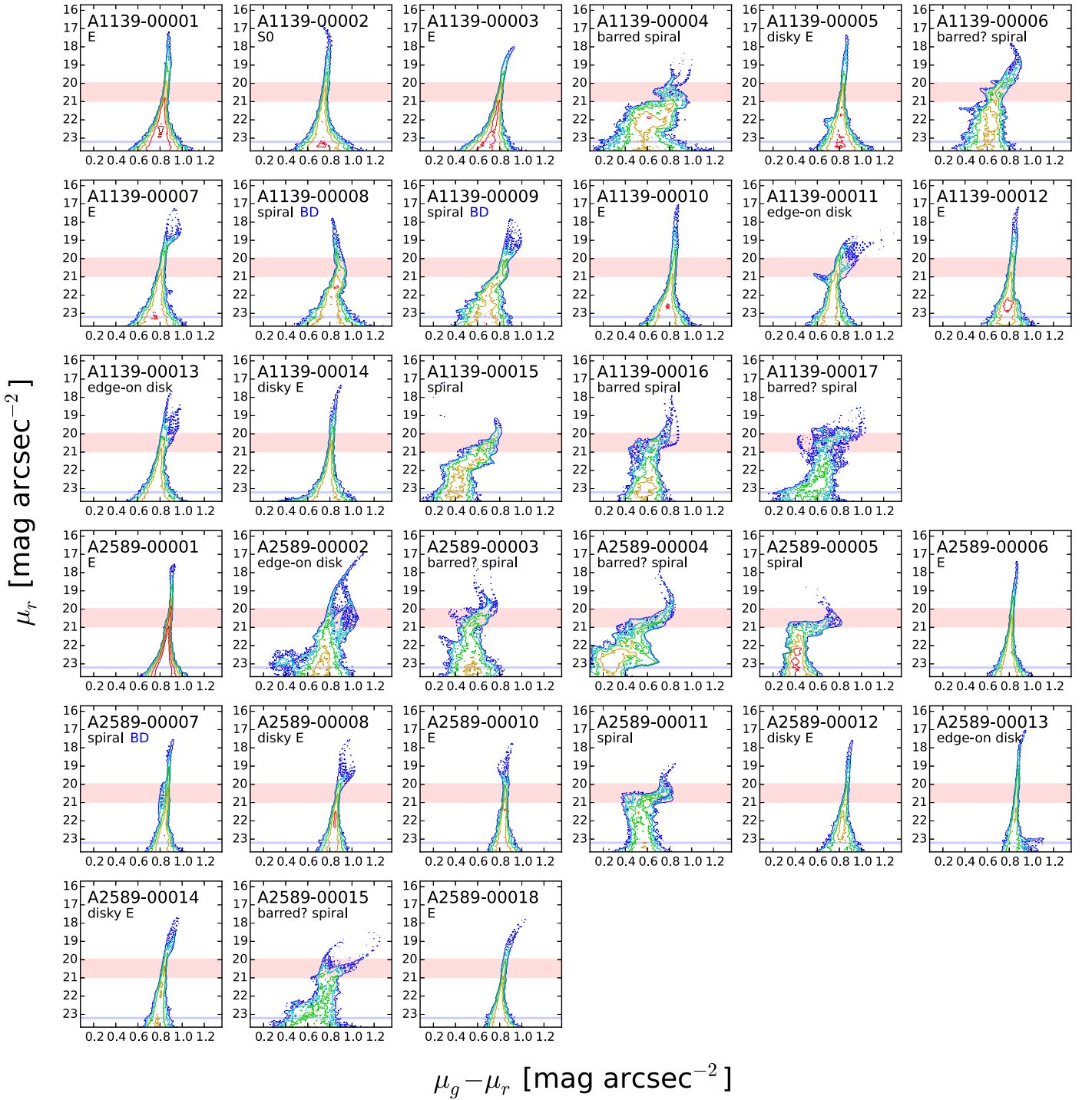


Figure 8. Log-scale pixel number density contours of the final pCMDs after the alternative masking procedure. The $20.0 \leq \mu_r \leq 21.0$ mag arcsec $^{-2}$ range (faint red stripe) and the $\mu_r = 23.2$ mag arcsec $^{-2}$ limit (faint blue line) are denoted.

4.2.1. Reliability Limits

Following Lee et al. (2017), we limit our analysis to $\mu_r \leq 23.2$ mag arcsec $^{-2}$ for the use of pixel color, at which the photometric uncertainty of a single pixel is smaller than 0.03 mag arcsec $^{-2}$. On the other hand, the limit for the use of pixel color dispersion⁹ ($\sigma(g - r)$) is $\mu_r \leq 21.2$ mag arcsec $^{-2}$.

⁹ In this paper, the term “color dispersion” indicates the standard deviation of pixel colors at given μ_r . This quantity was called “color deviation” in Lee et al. (2017), but we replace it by “color dispersion” for better understanding.

At $\mu_r > 21.2$ mag arcsec $^{-2}$, color dispersion tends to be significantly affected by the photometric uncertainty of individual pixels and thus cannot represent the intrinsic scatter of pixel color (see Figure 11 of Lee et al. 2017).

When we compare color dispersion values, the consideration of photometric uncertainty is important even at $\mu_r \leq 21.2$ mag arcsec $^{-2}$, depending on the situation. Lee et al. (2017) empirically showed that the lower limit of reliable color dispersion at given μ_r is $1.3 \times$ the photometric uncertainty of a single pixel in A1139 and A2589. For example, if a $\max(\sigma(g - r))_{20.0 \leq \mu_r \leq 21.0}$

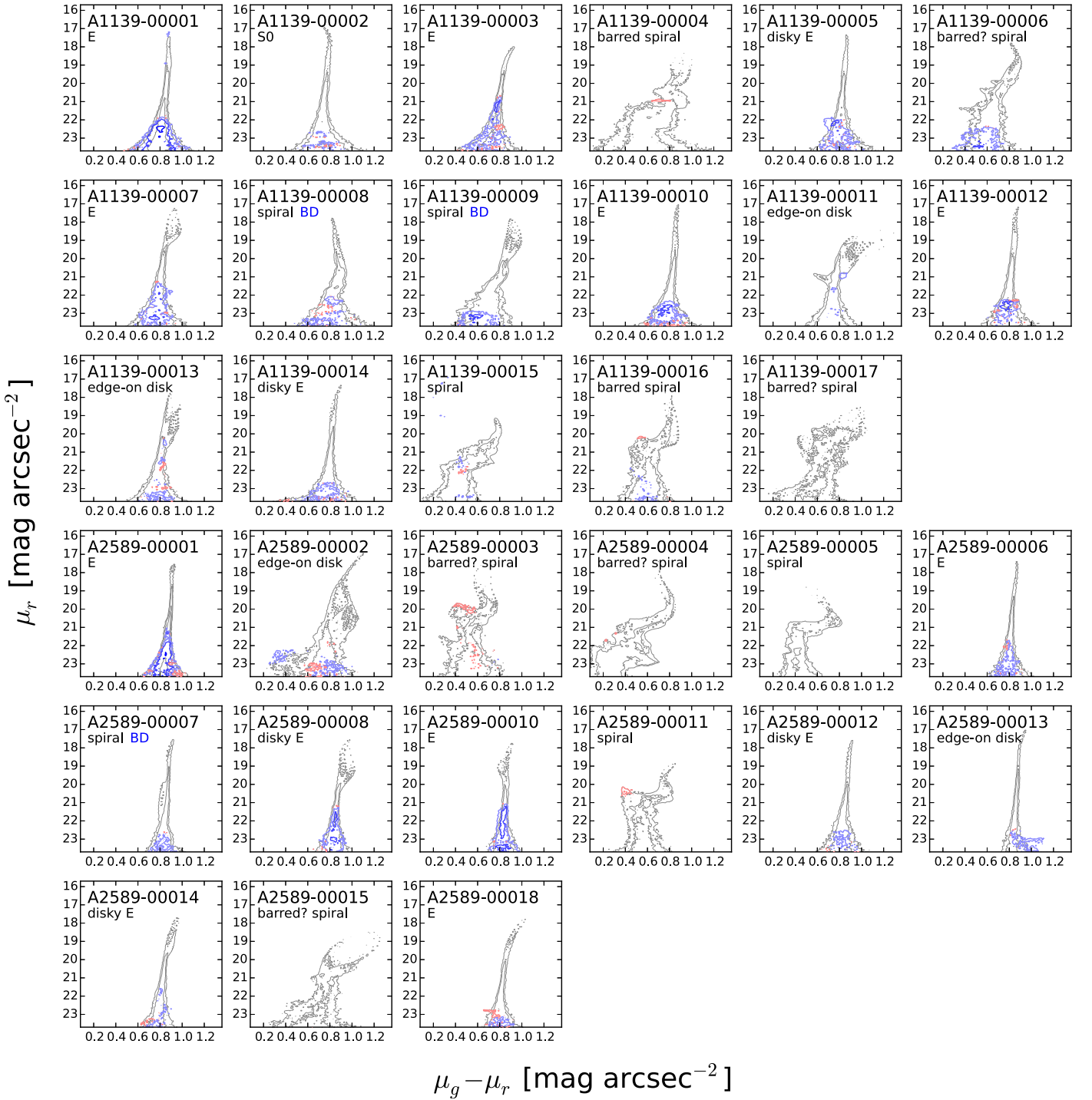


Figure 9. Log-scale contours of the difference in pixel number density of pCMDs between the two masking procedures (Figure 7 subtracted by Figure 8). The red contours indicate the domain at which the pCMDs after the standard masking procedure are denser (Figure 7 > 8), whereas the blue contours show the opposite case (Figure 7 < 8). The gray contours show the pCMDs after the standard masking procedure.

value is close to the value of $1.3 \times$ the typical photometric uncertainty at $\mu_r = 21.0 \text{ mag arcsec}^{-2}$, then the measured $\max(\sigma(g-r))_{20.0 \leq \mu_r \leq 21.0}$ value indicates the upper limit rather than the intrinsic color dispersion. In other words, we can regard the color dispersion to be intrinsic only when the value is sufficiently larger than $1.3 \times$ the photometric uncertainty.

This should be also considered when we compare $\min(\sigma(g-r))_{\mu_r \leq 21.2}$. Although the minimum color dispersion usually corresponds to that at the brightest μ_r ($\mu_r(\text{tip})$) and the

photometric uncertainty of the brightest pixel is typically tiny, the reliability limit needs to be accounted for if the measured color dispersion is also very small. Because the faintest surface brightness among the brightest pixels of our sample galaxies (i.e., maximum $\mu_r(\text{tip})$) is about $19.2 \text{ mag arcsec}^{-2}$, we can safely regard the $\min(\sigma(g-r))_{\mu_r \leq 21.2}$ value to be intrinsic if it is larger than $1.3 \times$ the photometric uncertainty at $\mu_r = 19.2 \text{ mag arcsec}^{-2}$. Hereafter, all interpretations of the figures are based on these considerations.

Table 2
Parameters Describing pCMD Features

pCMD Parameter	Description
$\mu_r(\text{tip})$	Minimum (brightest) r -band surface brightness among all pixels
$\min(g - r)_{\mu_r \leq 23.2}$	Minimum (bluest) value of mean $g - r$ color at $\mu_r \leq 23.2$ mag arcsec ⁻²
$\max(g - r)_{\mu_r \leq 23.2}$	Maximum (reddest) value of mean $g - r$ color at $\mu_r \leq 23.2$ mag arcsec ⁻²
$\min(\sigma(g - r))_{\mu_r \leq 21.2}$	Minimum (tightest) value of $g - r$ color dispersion at $\mu_r \leq 21.2$ mag arcsec ⁻²
$\max(\sigma(g - r))_{\mu_r \leq 21.2}$	Maximum (most dispersed) value of $g - r$ color dispersion at $\mu_r \leq 21.2$ mag arcsec ⁻²
$\max(\sigma(g - r))_{20.0 \leq \mu_r \leq 21.0}$	Maximum value of $g - r$ color dispersion at $20.0 \leq \mu_r \leq 21.0$ mag arcsec ⁻²
$\max(\sigma(g - r))_{18.5 \leq \mu_r \leq 19.5}$	Maximum value of $g - r$ color dispersion at $18.5 \leq \mu_r \leq 19.5$ mag arcsec ⁻²

Note. The “mean $g - r$ color” and “ $g - r$ color dispersion” indicate the quantities estimated using the pixels with fixed μ_r . That is, $\min(g - r)_{\mu_r \leq 23.2}$ is the bluest value among the “mean $g - r$ colors as a function of μ_r ,” not the $g - r$ color of the bluest pixel among the whole pixels. In the text, “the minimum (maximum) $g - r$ color” indicates “the minimum (maximum) value of mean $g - r$ color as a function of μ_r .”

4.2.2. Galaxy Morphology and pCMD Parameters

We now investigate the relationship between the pCMD parameters and galaxy morphology, and its physical implication. Figure 10 presents the basic correlations between the pCMD parameters, with the morphological types denoted. The trends between the parameters in the whole sample are mostly not obvious, but Figure 10(b) shows a notable anti-correlation between $\min(g - r)_{\mu_r \leq 23.2}$ and $\max(\sigma(g - r))_{20.0 \leq \mu_r \leq 21.0}$. This anti-correlation appears to be closely related with galaxy morphology, in the context that elliptical galaxies tend to have larger $\min(g - r)_{\mu_r \leq 23.2}$ and smaller $\max(\sigma(g - r))_{20.0 \leq \mu_r \leq 21.0}$ than galaxies of other types. This is a quantitative expression of the fact that the elliptical galaxies hardly have blue pixels and their pCMDs tend to be tightly bound.

A similar plot was shown in Figure 13 of Lanyon-Foster et al. (2007), in which the mean pixel color and the mean pixel color dispersion were compared. Although Lanyon-Foster et al. found a correlation between those mean values, its scatter was larger than that in our Figure 10(b). This indicates that the minimum pixel color and the maximum pixel color dispersion are better indicators of galaxy morphology than the mean values. On the other hand, the minimum pixel color dispersion (Figure 10(a)) or the maximum pixel color (Figures 10(c)–(d)) seems to be less efficient even than the mean values. The reason is not difficult to understand: even late-type galaxies may have small $\min(\sigma(g - r))$ values due to their bulges, and large $\max(g - r)$ values due to significant dust extinction in their disks as well as in their bulges.

In Figure 11, we examine how well galaxy morphology is distinguished by pCMD colors and $\mu_r(\text{tip})$. In Figure 11(a), the elliptical galaxies are distributed in a small domain, whereas the spiral galaxies show a much wider distribution. Most spiral galaxies tend to have pixel colors bluer than those of early-type galaxies, but the $\max(g - r)_{\mu_r \leq 23.2}$ values of some late-type galaxies are similar (A1139-00017 and A1139-00006) or even larger (A2589-00015). On the other hand, $\min(g - r)_{\mu_r \leq 23.2}$ seems to divide elliptical galaxies from spiral galaxies better than $\max(g - r)_{\mu_r \leq 23.2}$ does, except for bulge-dominated spiral galaxies (A1139-00008 and A2589-00007) and edge-on disk galaxies. This is because $\max(g - r)_{\mu_r \leq 23.2}$ represents the color of a late-type galaxy’s bulge, which is known to be similar to an elliptical galaxy in its properties (Dressler 1987; Fisher & Drory 2008),¹⁰ whereas $\min(g - r)_{\mu_r \leq 23.2}$ is strongly affected by the disk

parts. In Figure 11(b), the $\mu_r(\text{tip})$ is brighter than 18.0 mag arcsec⁻² for all elliptical galaxies in our sample. On the other hand, many spiral galaxies have fainter $\mu_r(\text{tip})$, but some have $\mu_r(\text{tip})$ as bright as those of elliptical galaxies (A2589-00003 and A2589-00004). These results show that the combination of pCMD colors and $\mu_r(\text{tip})$ moderately divides early- and late-type galaxies, albeit not perfectly.

Next, we test the capability of pCMD color dispersion parameters to classify galaxy morphology in Figure 12. The combination of color dispersion divides early- and late-type galaxies as nicely as or even better than the color index combination does. This indicates that the complexity of stellar populations at given μ_r as well as their mean age and metallicity is an important feature discriminating between early- and late-type galaxies. After examining various combinations, we found that the best combination to discriminate galaxy morphology is $\min(\sigma(g - r))_{\mu_r \leq 21.2}$ and $\max(\sigma(g - r))_{20.0 \leq \mu_r \leq 21.0}$. In Figure 12(b) (zoomed-in in Figure 13(a)), the elliptical galaxies are well separated from the spiral galaxies, and even from the bulge-dominated spiral galaxies, unlike in Figure 11. This seems to be mainly because $\max(\sigma(g - r))_{20.0 \leq \mu_r \leq 21.0}$ represents how complex the stellar populations are at the region where the disk component starts to surpass the bulge component in a typical late-type galaxy. It consequently reflects the disk dominance in a galaxy, because stellar populations in a disk tend to be much more complex than those in a bulge. See the plots in the second row of Figure 6 (and Appendix A) for the spatial areas covered by the pixels with $20.0 \leq \mu_r \leq 21.0$ in each galaxy.

However, although the $\min(\sigma(g - r))_{\mu_r \leq 21.2}$ versus $\max(\sigma(g - r))_{20.0 \leq \mu_r \leq 21.0}$ plot seems to distinguish early-type (E, disk E, and S0) galaxies from spiral galaxies almost perfectly, the edge-on disk galaxies are still mixed with the elliptical galaxies in this plot. To distinguish them, a parameter that is not from a pCMD is necessary: the axis ratio (b/a). Figure 12(d) (zoomed-in in Figure 13(b)) shows that the edge-on disk galaxies are separated from the early-type galaxies in the b/a versus $\max(\sigma(g - r))_{20.0 \leq \mu_r \leq 21.0}$ plot, due to their small b/a values. In summary, at least in our sample, the early-type galaxies are well distinguished from the other galaxies in the parameter space of $\min(\sigma(g - r))_{\mu_r \leq 21.2}$, $\max(\sigma(g - r))_{20.0 \leq \mu_r \leq 21.0}$, and axis ratio. The pCMDs from the alternative masking procedure also give consistent results (Appendix B).

In Figure 14, we compare the pCMD color dispersion parameters with B/T, one of the most frequently used indicators of galaxy morphology. The performance of B/T for morphological classification is not bad: the elliptical and

¹⁰ However, see also Gadotti (2009).

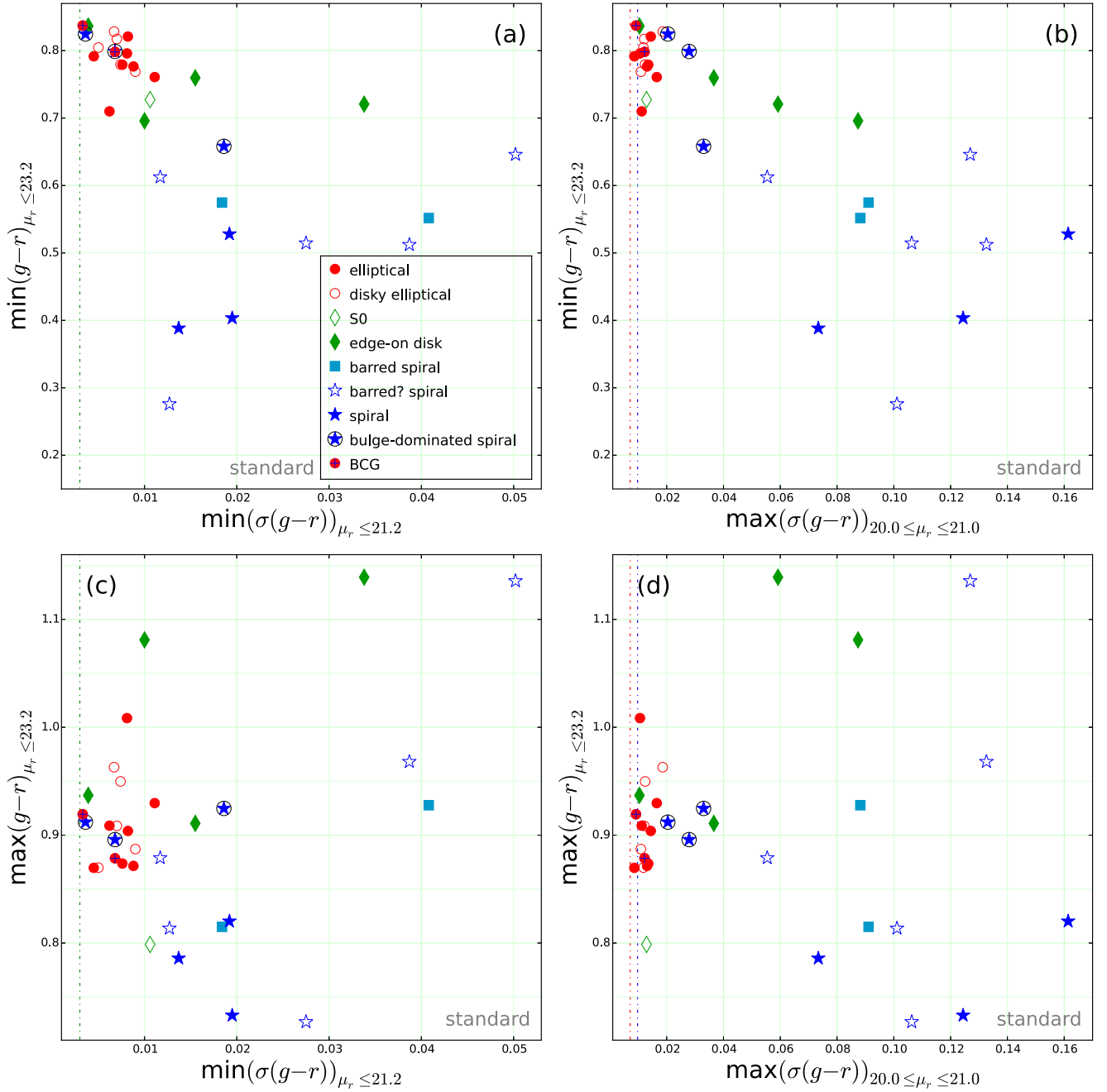


Figure 10. Correlations between pCMD parameters, based on the pCMDs after the standard procedure: (a) the minimum $g - r$ color at $\mu_r \leq 23.2$ mag arcsec $^{-2}$ vs. the minimum $g - r$ color dispersion at $\mu_r \leq 21.2$ mag arcsec $^{-2}$, (b) the minimum $g - r$ color at $\mu_r \leq 23.2$ mag arcsec $^{-2}$ vs. the maximum $g - r$ color dispersion at $20.0 \leq \mu_r \leq 21.0$ mag arcsec $^{-2}$, (c) the maximum $g - r$ color at $\mu_r \leq 23.2$ mag arcsec $^{-2}$ vs. the minimum $g - r$ color dispersion at $\mu_r \leq 21.2$ mag arcsec $^{-2}$, and (d) the maximum $g - r$ color at $\mu_r \leq 23.2$ mag arcsec $^{-2}$ vs. the maximum $g - r$ color dispersion at $20.0 \leq \mu_r \leq 21.0$ mag arcsec $^{-2}$. The dotted-dashed lines represent the lower limits of color dispersion, above which it is dominated by intrinsic color scatter rather than photometric uncertainty, at 21.0 mag arcsec $^{-2}$ for A1139 (blue; in panels (b) and (d)), at 21.0 mag arcsec $^{-2}$ for A2589 (red; in panels (b) and (d)), and at 19.2 mag arcsec $^{-2}$ for both clusters (green; in panels (a) and (c)).

spiral galaxies are mostly separated by B/T. However, it fails to distinguish between elliptical galaxies and bulge-dominated spiral galaxies. Since $\max(\sigma(g - r))_{20.0 \leq \mu_r \leq 21.0}$ even distinguishes between these galaxies, B/T appears to perform more poorly than color dispersion. Note that the structural decomposition may be improved if one makes more effort, such as a more careful setup of masks and better initial guess, and more various component-functions for more realistic fitting (Peng et al. 2010; Kim et al. 2016). However, the possibility of improvement in structural decomposition in this way inversely

highlights the strength of the pCMD approach, which is simple and is negligibly dependent on such technical conditions.

4.3. Dependence on WISE Color

Another main purpose of this paper is to understand the relationship between stellar population complexity and recent star formation activity in a galaxy. While the former is measured by the pCMD color dispersion, we use photometric information in the infrared bands to estimate the star formation activities of the target galaxies.

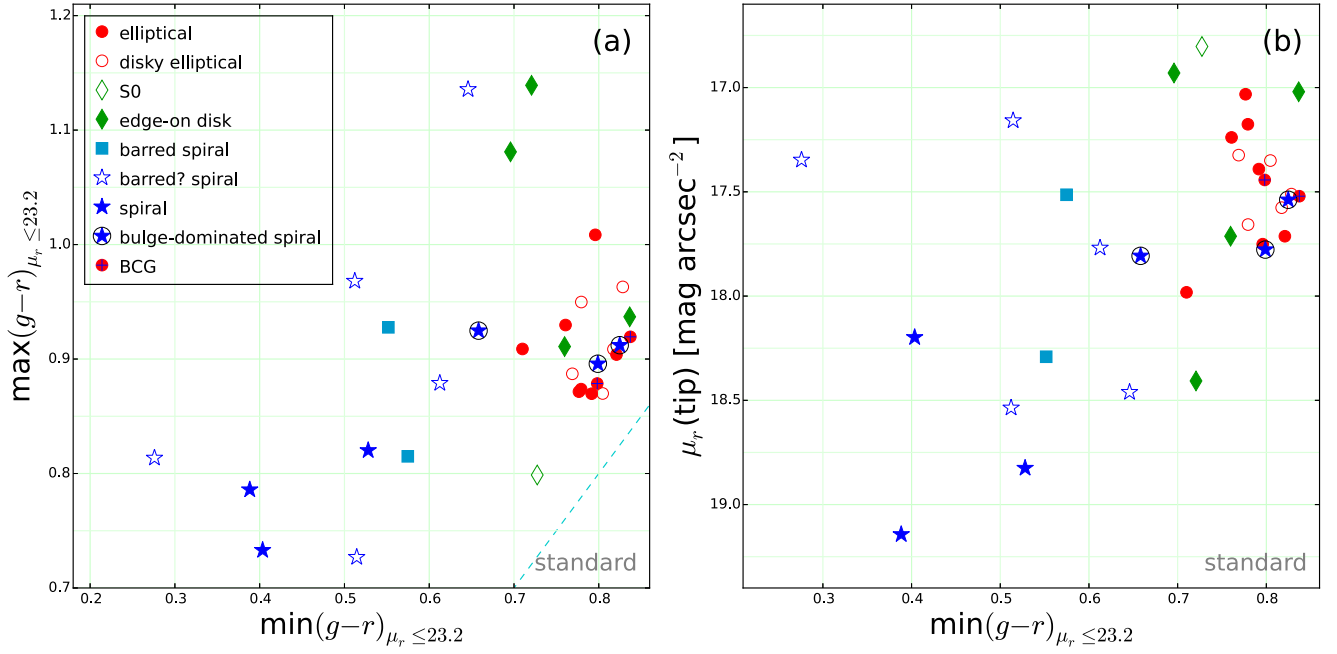


Figure 11. (a) Maximum vs. minimum values of mean $g - r$ color at $\mu_r \leq 23.2$ mag arcsec $^{-2}$, and (b) the brightest μ_r vs. the minimum $g - r$ color at $\mu_r \leq 23.2$ mag arcsec $^{-2}$, based on the pCMDs after the standard masking procedure. The various symbols indicate the morphological types, and the dashed line (cyan) shows the one-to-one relation.

Jarrett et al. (2017) showed how the infrared color-color ([3.4]–[4.6] versus [4.6]–[12]) diagram classifies galaxies according to their star formation and AGN activities. Based on the scheme, Figure 15 shows that the morphological types of our sample galaxies are strongly correlated with their star formation activities. While all of our sample galaxies are in the non-AGN domain ([3.4]–[4.6] < 0.8), the spiral galaxies are clearly redder (more active star formation) than the elliptical galaxies in the [4.6]–[12] color, except for two bulge-dominated spiral galaxies. Edge-on disk galaxies are in the intermediate domain between elliptical and spiral galaxies, although several elliptical galaxies and two bulge-dominated spiral galaxies also share that domain. Note that the edge-on disk galaxies in our sample tend to be bulge-dominated rather than disk-dominated, and thus they may be intrinsically similar to bulge-dominated spiral galaxies.

In Figure 16, we compare the pCMD parameters and the total infrared colors of the sample galaxies. There is a strong correlation between [4.6]–[12] and $\min(g - r)_{\mu_r \leq 23.2}$, whereas $\max(g - r)_{\mu_r \leq 23.2}$ shows no clear correlation with [4.6]–[12]. The former trend is as expected, because blue optical color and red infrared color are commonly the signals of star formation activity. Since star-forming spiral galaxies often have red bulges, the latter trend is also understood. However, when we consider the elliptical galaxies only, no significant correlation is found between [4.6]–[12] and $\min(g - r)_{\mu_r \leq 23.2}$. That is, the elliptical galaxies with small excess in infrared color show no difference in $\min(g - r)_{\mu_r \leq 23.2}$ from those without infrared-color excess. On the other hand, for the elliptical galaxies, $\min(\sigma(g - r))_{\mu_r \leq 21.2}$ and $\max(\sigma(g - r))_{20.0 \leq \mu_r \leq 21.0}$ appear to be correlated with [4.6]–[12]: the elliptical galaxies with larger [4.6]–[12] tend to have larger $\min(\sigma(g - r))_{\mu_r \leq 21.2}$ and $\max(\sigma(g - r))_{20.0 \leq \mu_r \leq 21.0}$, as shown in panels (c) and (d) of Figure 16.

The Pearson correlation coefficients and their p -values between several pCMD parameters and the *WISE* color are listed in Table 3. This table quantitatively shows that $\min(g - r)_{\mu_r \leq 23.2}$,

$\min(\sigma(g - r))_{\mu_r \leq 21.2}$, and $\max(\sigma(g - r))_{20.0 \leq \mu_r \leq 21.0}$ are significantly correlated or anti-correlated with [4.6]–[12], whereas $\max(g - r)_{\mu_r \leq 23.2}$ shows no significant correlation for the whole sample. On the other hand, such trends are somewhat different when only elliptical galaxies are considered: $\min(\sigma(g - r))_{\mu_r \leq 21.2}$ shows a marginal correlation and $\max(\sigma(g - r))_{20.0 \leq \mu_r \leq 21.0}$ shows a stronger correlation. It is also noted that $\max(g - r)_{\mu_r \leq 23.2}$ has a marginal correlation with [4.6]–[12] when elliptical and disky elliptical galaxies are considered together, while it has an anti-correlation when spiral galaxies are considered only. None of these trends significantly changes even when we use the results from the alternative procedure (Appendix B).

Table 4 lists the pCMD parameter values of the sample galaxies from the standard procedure and their *WISE* colors, which are used in Figures 10–16. The *WISE* colors used in Appendix B are the same as those in Table 4.

5. Discussion

5.1. Issues on Masking

There are some fundamental difficulties in masking contaminants. In the case of early-type galaxies or edge-on disk galaxies, the masking is relatively easy: SE-detection-based masking works well, because those galaxies have hardly any confusing internal substructures. After SE-detection-based masking, possible remaining contaminants will be covered by the pCMD outlier masking, although it may sometimes over-mask internal substructures such as tidal debris.

What does matter is masking in late-type galaxies. Basically, it is very difficult to perfectly mask contaminants in and around a face-on, late-type galaxy with complex spiral arms, because its substructures and contaminants are often too similar to be distinguished. Thus, in the standard procedure, we omitted SE-detection-based masking for such targets, and only conducted pCMD outlier masking, which works alone to some extent. However, this means that different masking processes are

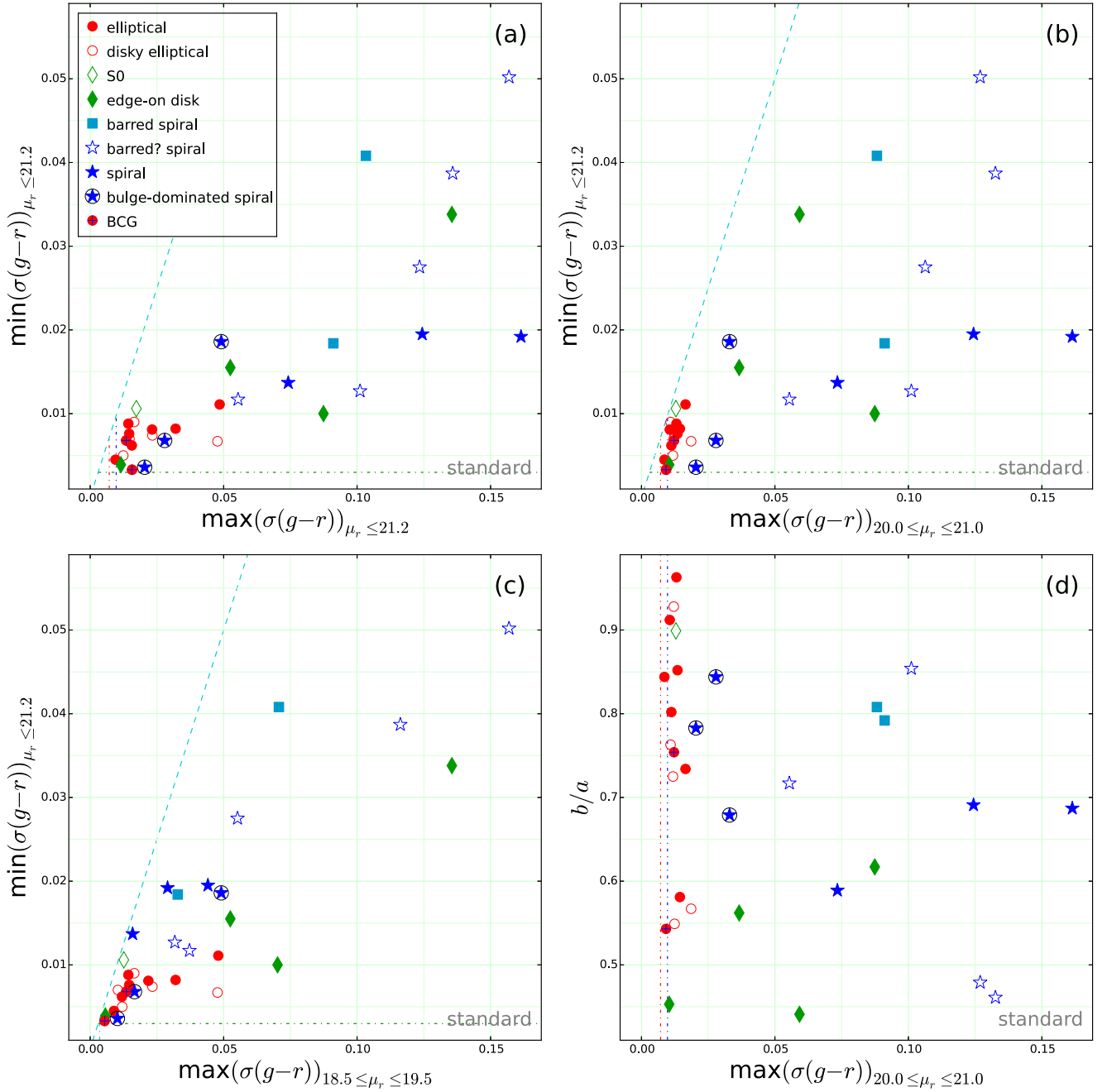


Figure 12. Minimum $g-r$ color dispersion at $\mu_r \leq 21.2$ mag arcsec $^{-2}$ vs. the maximum $g-r$ color dispersion at (a) $\mu_r \leq 21.2$ mag arcsec $^{-2}$, (b) $20.0 \leq \mu_r \leq 21.0$ mag arcsec $^{-2}$, and (c) $18.5 \leq \mu_r \leq 19.5$ mag arcsec $^{-2}$. (d) Axis ratio vs. the maximum $g-r$ color dispersion at $20.0 \leq \mu_r \leq 21.0$ mag arcsec $^{-2}$. The dashed lines (cyan) show the one-to-one relations. The blue, red, and green dotted-dashed lines are the reliability limits as described in Figure 10, and the cyan vertical dotted-dashed line in panel (c) is the lower limit at 19.5 mag arcsec $^{-2}$ for both clusters. All parameters are based on the pCMDs after the standard masking procedure.

applied to early- and late-type galaxies, which may cause inappropriate comparison of the pCMD features between galaxies with different morphological types.

The alternative masking procedure was devised to complement this weakness of the standard procedure. Through the alternative procedure, fair comparison is possible between galaxies of any morphological types. However, $R(\mu_r)$ -based masking is less efficient than SE-detection-based masking for early-type galaxies. It may fail to mask faint contaminants or those very close to the target galaxy center. Moreover, $R(\mu_r)$ -based masking may not cover the faint outskirts of a contaminating object due to the limit

of the masking algorithm. Thus, it is recommended to rely on the standard masking procedure if the sample consists of only early-type and edge-on galaxies. The main purpose of the alternative masking procedure is to check how reliable the results from the standard procedure are, by comparing them with the results from a self-consistent masking procedure.

Section 4.2.2 and Appendix B show that the results from the standard procedure and from the alternative procedure are not significantly different from each other. This is because our analysis in this paper focuses on the major trend in the pCMD of each galaxy rather than its fine features. The consistency between

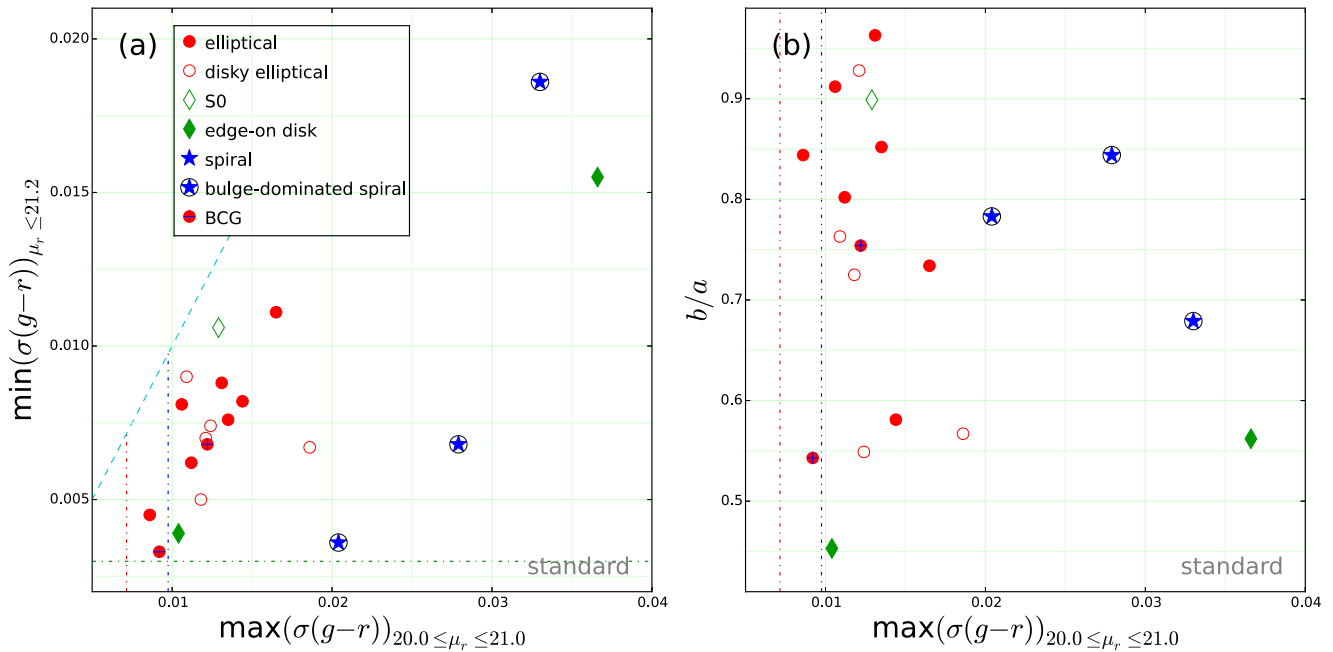


Figure 13. Zoom-in plots of (a) the minimum $g-r$ color dispersion at $\mu_r \leq 21.2$ mag arcsec $^{-2}$ vs. the maximum $g-r$ color dispersion at $20.0 \leq \mu_r \leq 21.0$ mag arcsec $^{-2}$ (Figures 12(b)), and (b) axis ratio vs. the maximum $g-r$ color dispersion at $20.0 \leq \mu_r \leq 21.0$ mag arcsec $^{-2}$ (Figure 12(d)). Both plots are based on the pCMDs after the standard masking procedure.

the results from the different procedures, despite the weakness of each masking procedure, indicates that the major trend of a pCMD is hardly influenced by the details of the masking methods.

5.2. Morphological Segregation

We tested various combinations of parameters measured from the pCMDs of our sample galaxies to examine how galaxies of different morphological types are quantitatively distinguished in their pCMD features. As a result, we found that the best parameter set to classify galaxy morphology based on pCMDs is a combination of the minimum color dispersion at $\mu_r \leq 21.2$ mag arcsec $^{-2}$ and the maximum color dispersion at $20.0 \leq \mu_r \leq 21.0$ mag arcsec $^{-2}$, assisted by axis ratio (Figure 13).

Although these parameters were empirically selected, the underlying mechanism in which they work is relatively easy to understand. As revealed in the pCMDs and the μ_r contour maps, $\max(\sigma(g-r))_{20.0 \leq \mu_r \leq 21.0}$ represents how complex the stellar populations are at the regions where the disk component begins to be dominant in a typical late-type galaxy. In other words, $\max(\sigma(g-r))_{20.0 \leq \mu_r \leq 21.0}$ is dominated by the bulge stellar populations for an early-type galaxy, whereas it is largely affected by the disk stellar populations for a late-type galaxy. That makes $\max(\sigma(g-r))_{20.0 \leq \mu_r \leq 21.0}$ a good indicator of disk dominance, because disks tend to have complex stellar populations that are spatially not uniform whereas bulges and elliptical galaxies have relatively uniform stellar populations.

Figure 17 shows 12 examples of radial profiles with structural decomposition using GALFIT, which partially supports this interpretation (but not perfectly). For galaxies with $B/T > 0.6$, the stellar populations at $20.0 \leq \mu_r \leq 21.0$ mag arcsec $^{-2}$ are dominated by bulge components; for galaxies with $B/T < 0.5$, the stellar populations at $20.0 \leq \mu_r \leq 21.0$ mag arcsec $^{-2}$ are affected more significantly by disk components.

Nevertheless, the bulge-disk decomposition does not completely explain the performance of $\max(\sigma(g-r))_{20.0 \leq \mu_r \leq 21.0}$, because there are some exceptional cases. For example, some bulge-dominated spiral galaxies (A1139-00009 and A2589-00007) have large B/T ratios and their stellar populations at $20.0 \leq \mu_r \leq 21.0$ mag arcsec $^{-2}$ seem to be dominated by their bulge components. Despite the fact that their B/T ratios are even larger than that of the S0 galaxy A1139-00002 (0.65 and 0.91 versus 0.61), their $\max(\sigma(g-r))_{20.0 \leq \mu_r \leq 21.0}$ values are also larger (0.036 and 0.020 versus 0.015). On the other hand, a disky elliptical galaxy A2589-00012 has a relatively small B/T (0.40), but its $\max(\sigma(g-r))_{20.0 \leq \mu_r \leq 21.0}$ is as small as 0.015. This indicates that the bulge-disk decomposition is not the only reason that $\max(\sigma(g-r))_{20.0 \leq \mu_r \leq 21.0}$ works. A spiral galaxy, even though it is extremely bulge-dominated (e.g., A2589-00007), seems to have more complex stellar populations compared to an early-type galaxy with a similar B/T ratio. That is, the pCMD color dispersion is a good indicator for detecting such a fine difference in stellar populations that is hardly caught in classical methods of structural decomposition.

Note that $\mu_r = 21.2$ mag arcsec $^{-2}$ is the analysis limit for color dispersion in our data and thus its performance at $\mu_r > 21.2$ mag arcsec $^{-2}$ cannot be probed in this paper. If deeper images with sufficient S/N even at $\mu_r > 21.2$ mag arcsec $^{-2}$ are used, the usefulness of color dispersion as an indicator of galaxy morphology may be even greater, because the photometric properties of the fainter part of a disk will be reflected. For example, in Figure 17, the disk component of A1139-00002 (S0) is small, but it becomes relatively dominant at $R > 10''$ (total $\mu_r \gtrsim 22.2$ mag arcsec $^{-2}$). Thus, it may be useful even in distinguishing between elliptical and S0 galaxies if the color dispersion at lower surface brightness is available.

On the other hand, $\min(\sigma(g-r))_{\mu_r \leq 21.2}$ represents the minimum complexity of stellar populations, typically (but not necessarily) at the brightest center. Although elliptical galaxies and bulges of late-type galaxies typically have simple

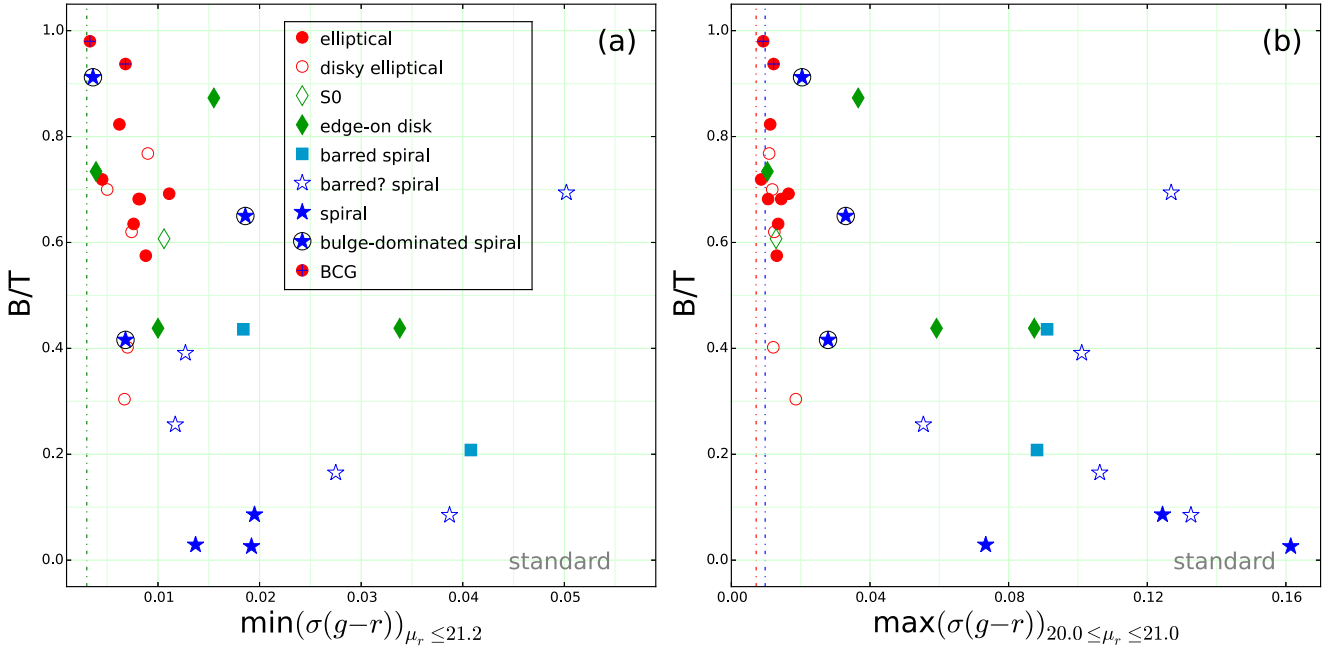


Figure 14. Comparison with bulge-to-total ratio (B/T) of (a) minimum $g - r$ color dispersion at $\mu_r \leq 21.2$ mag arcsec $^{-2}$ and (b) maximum $g - r$ color dispersion at $20.0 \leq \mu_r \leq 21.0$ mag arcsec $^{-2}$.

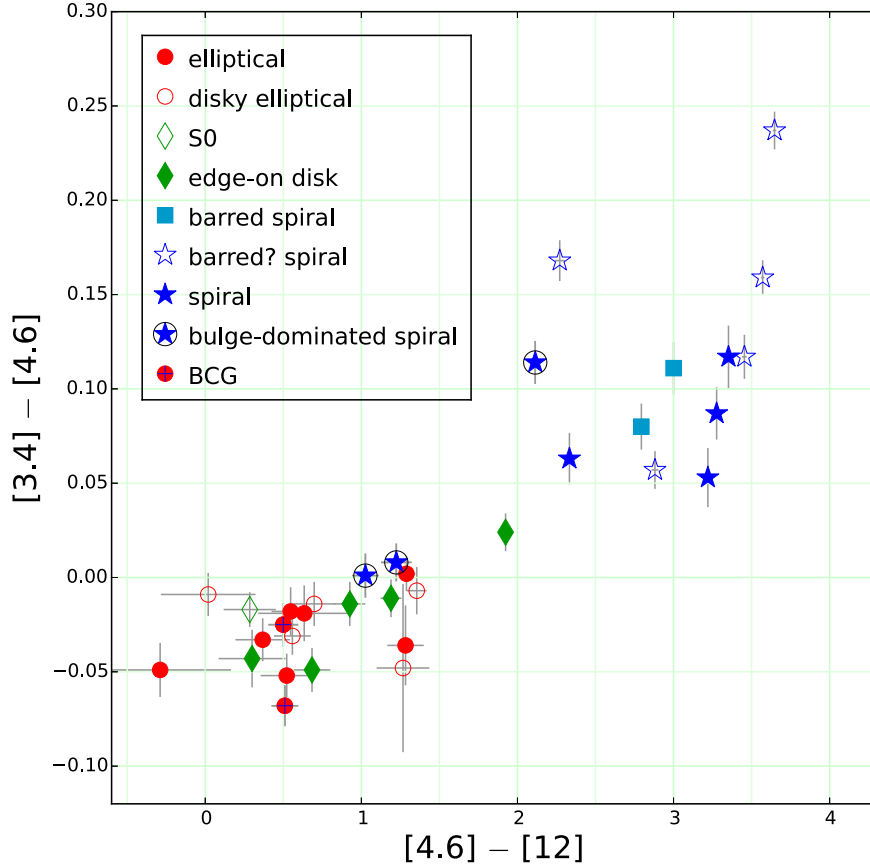


Figure 15. *WISE* infrared color-color diagram of the sample galaxies. Photometric uncertainties are denoted as gray lines for each target.

structures, they may show unusual substructures sometimes, which result in large color dispersions at their pCMD tips (e.g., A1139-00007 and A2589-00008). Since such substructures are thought to originate from mergers or interactions,

$\min(\sigma(g - r))_{\mu_r \leq 21.2}$ can be used as a simple indicator of recent mass assembly events of a target galaxy: a larger value giving a more complex history of recent mass assembly on average. This may not be a very precise indicator, but will be

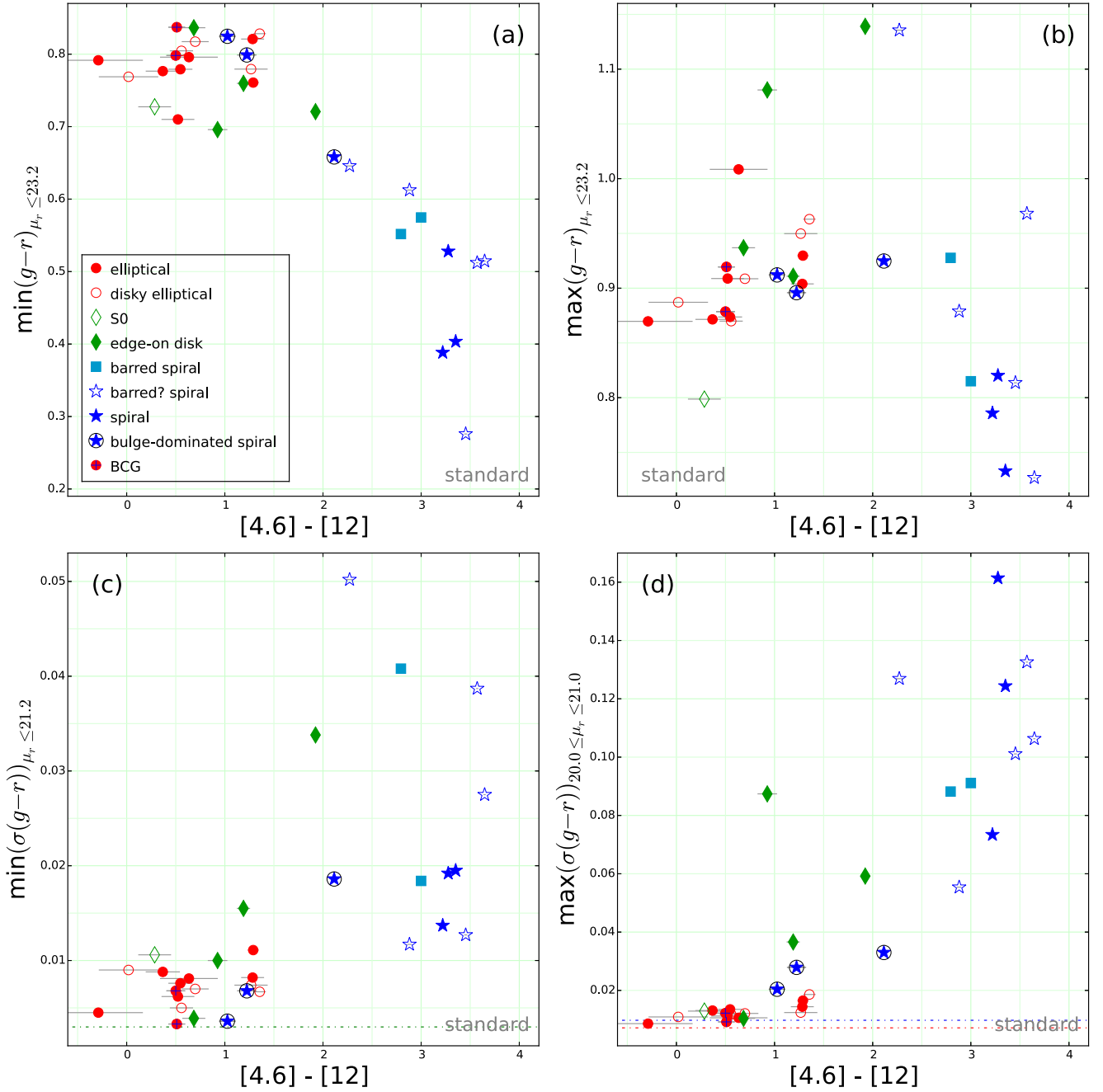


Figure 16. pCMD parameters vs. the *WISE* [4.6]–[12] color, based on the pCMDs after the standard masking procedure: (a) the minimum $g - r$ color at $\mu_r \leq 23.2$ mag arcsec $^{-2}$, (b) the maximum $g - r$ color at $\mu_r \leq 23.2$ mag arcsec $^{-2}$, (c) the minimum $g - r$ color dispersion at $\mu_r \leq 21.2$ mag arcsec $^{-2}$, and (d) the maximum $g - r$ color dispersion at $20.0 \leq \mu_r \leq 21.0$ mag arcsec $^{-2}$. The dotted–dashed lines are the reliability limits as described in Figure 10.

Table 3
Correlations with the *WISE* [4.6]–[12] Color

pCMD Parameters	All	E	E + disky E	Spirals
$\min(g - r)_{\mu_r \leq 23.2}$	−0.87 (0.000)	0.03 (0.935)	0.19 (0.506)	−0.62 (0.052)
$\max(g - r)_{\mu_r \leq 23.2}$	−0.25 (0.173)	0.37 (0.330)	0.54 (0.044)	−0.72 (0.019)
$\min(\sigma(g - r))_{\mu_r \leq 21.2}$	0.64 (0.000)	0.66 (0.052)	0.37 (0.190)	−0.44 (0.199)
$\max(\sigma(g - r))_{20.0 \leq \mu_r \leq 21.0}$	0.86 (0.000)	0.80 (0.010)	0.77 (0.001)	0.19 (0.602)

Note. Pearson correlation coefficients (and p -values) with the *WISE* [4.6]–[12] color, for all galaxies (All; 32), elliptical galaxies (E; 9), elliptical + disky elliptical galaxies (E + disky E; 14), and barred + unbarred spiral galaxies (Spirals; 13), based on the pCMDs after the standard masking procedure.

Table 4
pCMD Parameters from the Standard Procedure, and *WISE* Colors

Name	$\min(g - r)$ $\mu_r \leq 23.2$	$\max(g - r)$ $\mu_r \leq 23.2$	$\mu_r(\text{tip})$	$\min(\sigma(g - r))$ $\mu_r \leq 21.2$	$\max(\sigma(g - r))$ $20.0 \leq \mu_r \leq 21.0$	$\max(\sigma(g - r))$ $18.5 \leq \mu_r \leq 19.5$	$\max(\sigma(g - r))$ $\mu_r \leq 21.2$	[3.4]–[4.6]	[4.6]–[12]
A1139-00001	0.798	0.879	17.44	0.007	0.012	0.013	0.013	-0.025 ± 0.012	0.500 ± 0.096
A1139-00002	0.727	0.799	16.80	0.011	0.013	0.013	0.017	-0.017 ± 0.009	0.285 ± 0.167
A1139-00003	0.710	0.909	17.98	0.006	0.011	0.012	0.016	-0.052 ± 0.012	0.522 ± 0.167
A1139-00004	0.552	0.928	18.29	0.041	0.088	0.071	0.103	0.080 ± 0.012	2.794 ± 0.026
A1139-00005	0.805	0.870	17.35	0.005	0.012	0.012	0.012	-0.031 ± 0.010	0.558 ± 0.118
A1139-00006	0.613	0.879	17.77	0.012	0.055	0.037	0.055	0.057 ± 0.010	2.881 ± 0.022
A1139-00007	0.761	0.930	17.24	0.011	0.017	0.048	0.049	0.002 ± 0.009	1.289 ± 0.057
A1139-00008	0.799	0.896	17.78	0.007	0.028	0.017	0.028	0.008 ± 0.010	1.224 ± 0.097
A1139-00009	0.658	0.925	17.81	0.019	0.033	0.049	0.049	0.114 ± 0.011	2.114 ± 0.032
A1139-00010	0.777	0.872	17.03	0.009	0.013	0.014	0.014	-0.033 ± 0.011	0.368 ± 0.174
A1139-00011	0.721	1.139	18.41	0.034	0.059	0.136	0.136	0.024 ± 0.010	1.924 ± 0.041
A1139-00012	0.779	0.874	17.18	0.008	0.013	0.015	0.015	-0.018 ± 0.013	0.547 ± 0.122
A1139-00013	0.760	0.911	17.71	0.015	0.037	0.052	0.052	-0.011 ± 0.010	1.190 ± 0.067
A1139-00014	0.769	0.887	17.32	0.009	0.011	0.017	0.017	-0.009 ± 0.011	0.019 ± 0.303
A1139-00015	0.388	0.786	19.14	0.014	0.073	0.016	0.074	0.053 ± 0.016	3.220 ± 0.021
A1139-00016	0.575	0.815	17.51	0.018	0.091	0.033	0.091	0.111 ± 0.014	3.000 ± 0.024
A1139-00017	0.512	0.968	18.54	0.039	0.133	0.116	0.136	0.159 ± 0.009	3.571 ± 0.011
A2589-00001	0.837	0.919	17.52	0.003	0.009	0.005	0.016	-0.068 ± 0.011	0.510 ± 0.085
A2589-00002	0.696	1.081	16.93	0.010	0.087	0.070	0.087	-0.014 ± 0.012	0.926 ± 0.100
A2589-00003	0.514	0.727	17.16	0.028	0.106	0.055	0.123	0.237 ± 0.010	3.647 ± 0.011
A2589-00004	0.276	0.814	17.35	0.013	0.101	0.032	0.101	0.117 ± 0.012	3.454 ± 0.016
A2589-00005	0.404	0.733	18.20	0.019	0.124	0.044	0.124	0.117 ± 0.017	3.352 ± 0.023
A2589-00006	0.792	0.870	17.39	0.004	0.009	0.009	0.009	-0.049 ± 0.014	-0.289 ± 0.454
A2589-00007	0.825	0.912	17.54	0.004	0.020	0.010	0.020	0.001 ± 0.012	1.026 ± 0.085
A2589-00008	0.828	0.963	17.51	0.007	0.019	0.048	0.048	-0.007 ± 0.013	1.355 ± 0.063
A2589-00010	0.821	0.904	17.71	0.008	0.014	0.032	0.032	-0.036 ± 0.021	1.283 ± 0.117
A2589-00011	0.528	0.820	18.82	0.019	0.161	0.029	0.161	0.087 ± 0.014	3.276 ± 0.024
A2589-00012	0.817	0.909	17.58	0.007	0.012	0.010	0.015	-0.014 ± 0.012	0.698 ± 0.137
A2589-00013	0.837	0.937	17.02	0.004	0.010	0.006	0.011	-0.049 ± 0.012	0.684 ± 0.117
A2589-00014 ^a	0.779	0.950	17.66	0.007	0.012	0.023	0.023	-0.048 ± 0.045	1.267 ± 0.169
A2589-00015	0.646	1.136	18.46	0.050	0.127	0.157	0.157	0.168 ± 0.011	2.271 ± 0.033
A2589-00018	0.796	1.008	17.75	0.008	0.011	0.022	0.023	-0.019 ± 0.015	0.634 ± 0.294

Note.

^a The *WISE* colors of A2589-00014 are based on the profile-fit magnitudes, whereas those of all the other targets are based on the elliptical aperture magnitudes. See Section 2.3 for details.

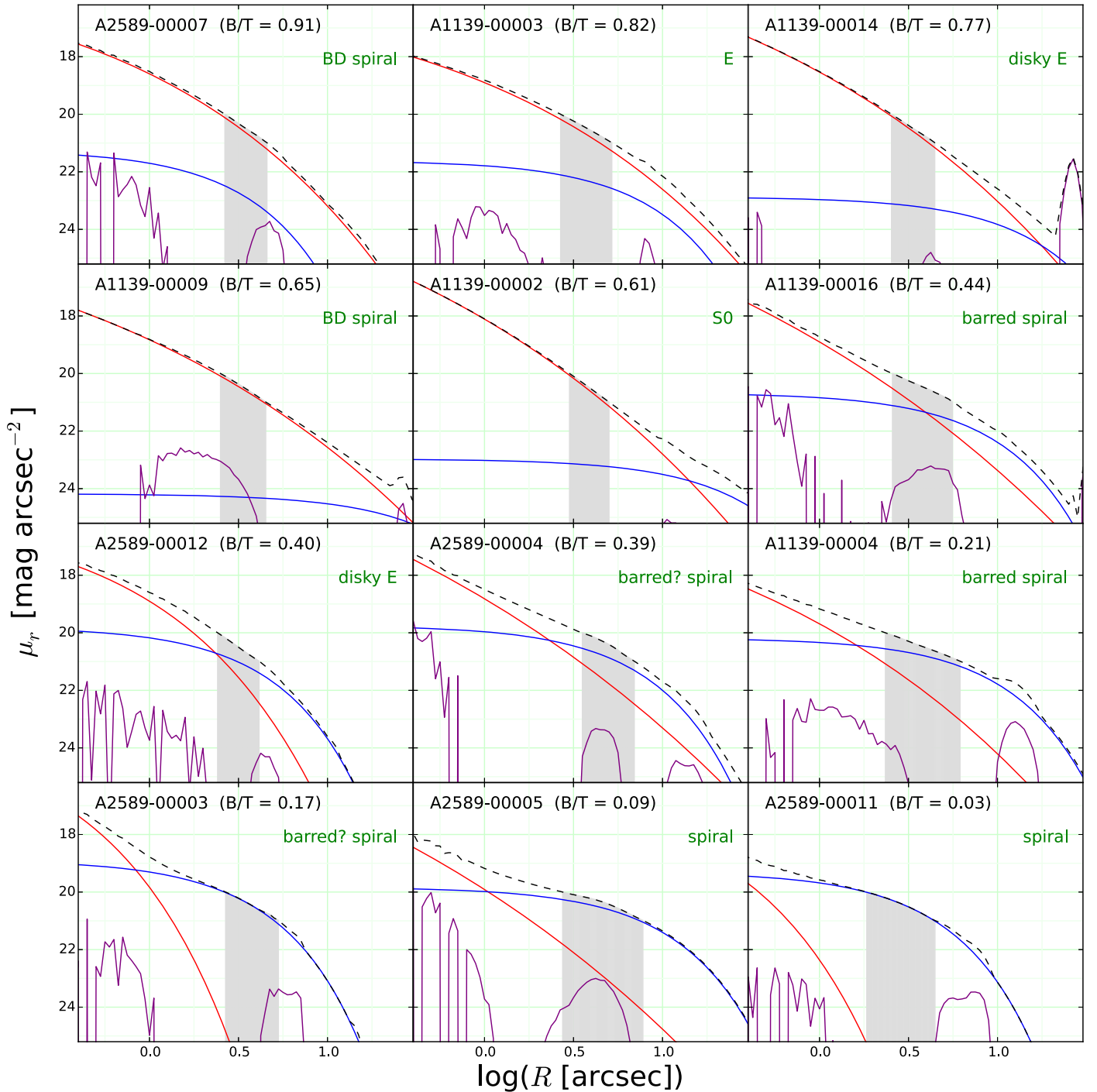


Figure 17. Radial profiles with structural decomposition using GALFIT, for 12 galaxies having various B/T ratios (0.03–0.91). Each galaxy is decomposed using a Sérsic component (bulge; red line) and an exponential component (disk; blue line). The purple line shows the residual light and the black dashed line is the total (bulge + disk + residual) profile in each panel. The radial regime corresponding to the total surface brightness between 20.0 and 21.0 mag arcsec⁻² is shaded on each plot.

useful particularly in a statistical study, because it can be conveniently applied to galaxies in bulk, if appropriate corrections are conducted for the difference in redshift and spatial resolution.

It is interesting that the best parameter to characterize galaxy morphology is color dispersion rather than color index itself. In other words, for morphological classification of galaxies, it is more effective to compare how well mixed the stellar populations are rather than to see how old or metal-rich on average they are. The latter also works to some extent, but it fails to discriminate

bulge-dominated spiral galaxies from elliptical galaxies in our results. This is not strange because the correlation between galaxy morphology and galaxy color is known to be not very tight (e.g., blue early-type galaxies and red late-type galaxies; Lee et al. 2006, 2008; Tojeiro et al. 2013).

However, for the generalized application of morphological classification using the pCMD features, additional work is required. First of all, a much larger number of galaxies with well-classified morphological types need to be tested to get more reliable criteria of morphological classification. Our sample size of

32 is absolutely insufficient to establish criteria that can be generally applied. Furthermore, it is necessary to examine how the criteria of morphological classification change as a function of image resolution. Since the pCMD features strongly depend on image resolution (Lee et al. 2011, 2012; Conroy & van Dokkum 2016), its effect on the pCMD classification should be seriously considered, in order to apply this method to galaxies at various redshifts. Nevertheless, if these issues are addressed, the pCMD classification method will be a valuable technique to automatically classify a huge number of galaxies in future imaging surveys using next-generation facilities such as the Large Synoptic Survey Telescope (Ivezic et al. 2008).

5.3. Recent Growth of Elliptical Galaxies

In Section 4.3, the elliptical galaxies show a marginal correlation between their $\min(\sigma(g-r))_{\mu_r \leq 21.2}$ and [4.6]–[12] (Figure 16(c)) and a stronger correlation between $\max(\sigma(g-r))_{20.0 \leq \mu_r \leq 21.0}$ and [4.6]–[12] (Figure 16(d)). Since the color dispersion reflects how complex stellar populations are in a galaxy, this result indicates that the elliptical galaxies with more complex stellar populations tend to have recently experienced more active star formation (or vice versa). According to some previous studies, the recent growth of massive elliptical galaxies mainly depends on dry mergers rather than gas-rich mergers (Naab et al. 2006; Kormendy et al. 2009; Bernardi et al. 2011). On the other hand, some other studies found evidence of recent star formation activity probably triggered by mergers in some massive elliptical galaxies (Kaviraj et al. 2009; Fernández-Ontiveros et al. 2011; Sheen et al. 2016). Our result supports the latter findings: the recent star formation activity and mass growth of massive elliptical galaxies appear to be correlated with each other in our sample. Thus, the recent growth of those elliptical galaxies may not entirely depend on dry mergers, and gas-rich minor mergers may have occurred.

One may suspect that the complexity of stellar populations in those galaxies may not necessarily originate from merger events, but may be naturally caused by recent star formation not from merger origins. Even in that case, however, the recent star formation must have been spatially non-uniform at scales larger than 600 pc ($\sim 0''.8$ in our images) to enlarge the color dispersion in a pCMD. It may require anisotropic infall of gas. Gas interactions without disturbance of stellar orbits can be such an origin, which may occur even for cluster galaxies with high encounter velocities (Park & Hwang 2009). Although the exact origin of the recent star formation cannot be determined in this paper, it is plausible that some environmental effects acted on the large color dispersion in a pCMD.

The interpretation of the $\max(g-r)_{\mu_r \leq 23.2}$ versus [4.6]–[12] plot (Figure 16(b)) is somewhat complicated. At first glance, the data points seem to be randomly scattered in this plot. However, as shown in Table 3, we find two opposite trends when we inspect the subsamples of the elliptical + disk elliptical galaxies and the spiral galaxies: the elliptical galaxies with infrared-color excess tend to have redder maximum pCMD color, but the spiral galaxies are getting bluer in the optical band as infrared color increases.

These two opposite trends imply that multiple physical origins may be involved in the $\max(g-r)_{\mu_r \leq 23.2}$ versus [4.6]–[12] relation. For example, the marginal correlation of elliptical + disk elliptical galaxies may result from dust remnants in some elliptical galaxies. That is, elliptical galaxies that have recently experienced star formation may have remaining dust,

which cause red infrared color (due to remaining warm dust) and red optical color (by dust extinction) at the same time. On the other hand, spiral galaxies with redder infrared color may have more active current star formation, unlike elliptical galaxies, and thus they tend to have blue optical color due to a large amount of young stars that cannot be sufficiently obscured by dust. It will be worth checking if these trends are maintained in a sufficiently large sample of galaxies in future studies.

6. Conclusion

We analyzed the pixel color–magnitude diagrams (pCMDs) of 32 bright galaxies in two galaxy clusters, A1139 and A2589, at low redshifts. We yielded the pCMDs of the sample galaxies using SE-detection-based masking or $R(\mu_r)$ -based masking, either of which is complemented by the subsequent pCMD outlier masking process. We compared the results from the two procedures with each other, and confirmed that the different masking methods do not significantly affect the major trends of pCMD properties.

Our main conclusions from the pCMD analysis of the target galaxies are as follows.

1. At least in our sample, the early- and late-type galaxies are most clearly separated by the combination of the minimum color dispersion at $\mu_r \leq 21.2$ mag arcsec⁻² and the maximum color dispersion at $20.0 \leq \mu_r \leq 21.0$ mag arcsec⁻², while the edge-on galaxies are discriminated using axis ratio. This is because $\min(\sigma(g-r))_{\mu_r \leq 21.2}$ represents the minimum complexity of stellar populations typically at the brightest center, whereas $\max(\sigma(g-r))_{20.0 \leq \mu_r \leq 21.0}$ reflects the complexity of stellar populations at the disk component in a typical spiral galaxy.
2. The color dispersion measurements ($\min(\sigma(g-r))_{\mu_r \leq 21.2}$ and $\max(\sigma(g-r))_{20.0 \leq \mu_r \leq 21.0}$) of an elliptical galaxy appear to be correlated with its total infrared color ([4.6]–[12]). This indicates that the complexity of stellar populations in an elliptical galaxy is closely related with its recent star formation activity. From this observational evidence, we infer that gas-rich minor mergers or gas interactions may have usually occurred during the recent growth of massive elliptical galaxies.

In both conclusions, the color dispersion in a pCMD is a key quantity that appears to be closely related with the structure and formation history of a galaxy. Unlike the various pCMD features that are more complicated, such as the backbone curvature and the spatial distribution of outlying pixels (Lee et al. 2017), the color dispersion can be simply measured and applied to galaxies in bulk, to trace their recent formation histories. However, the definition and usage of this parameter need to be improved and more variously examined, because it must depend on rest-frame wavelength and spatial resolution of the target images. Our follow-up studies using the full sample of the KYDISC clusters will cover this topic.

We appreciate the anonymous referee who provided comments that were very helpful in improving this paper. In this work, we used the data obtained under the K-GMT Science Program funded through Korea GMT Project operated by Korea Astronomy and Space Science Institute (KASI). Parts of this research were conducted by the Australian Research Council Centre of Excellence for All Sky Astrophysics in 3 Dimensions (ASTRO 3D), through project number CE170100013.

Appendix A Full Plots in the Masking Processes

In Figure 6, we schematically summarized the masking processes in the standard and alternative procedures. However, the full plots showing the detailed masking processes for the whole sample galaxies were omitted to improve the readability of the paper. In this section, those full plots are presented.

The masking processes in the standard procedure flow as shown in Figures 18–20.

1. The target galaxies are masked using SE detection (Figure 18). SE-detection-based masking is adaptively applied with consideration of the morphology of a target galaxy and the performance of the masks. Among the 32 sample galaxies, 20 are masked using SE detection with both large and small background meshes (“Mm”), whereas eight are masked using SE detection only with large background meshes (“M”). The remaining four galaxies are not masked at all.

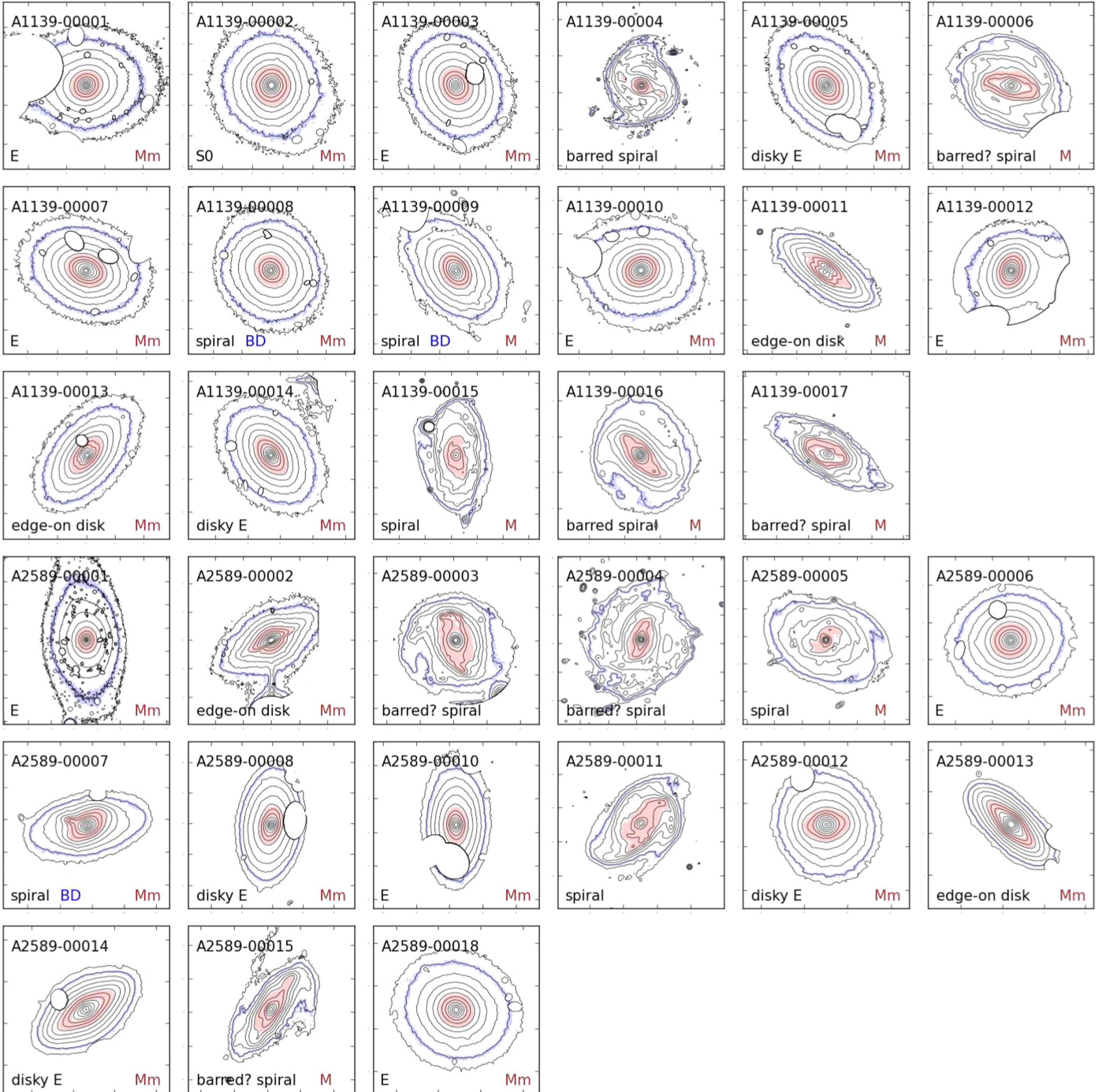


Figure 18. Surface brightness contour maps after SE-detection-based masking. The letters at the lower right corner indicate the type of masking: “M” indicates that the target galaxy was masked using SE detection with large background meshes only, while “Mm” indicates that the target galaxy was masked using SE detection with both large and small background meshes. The regions colored faintly red show the pixels with $20.0 \leq \mu_r \leq 21.0$ mag arcsec⁻², while the regions colored faintly blue denote the pixels on the analysis limit ($\mu_r = 23.2$ mag arcsec⁻²).

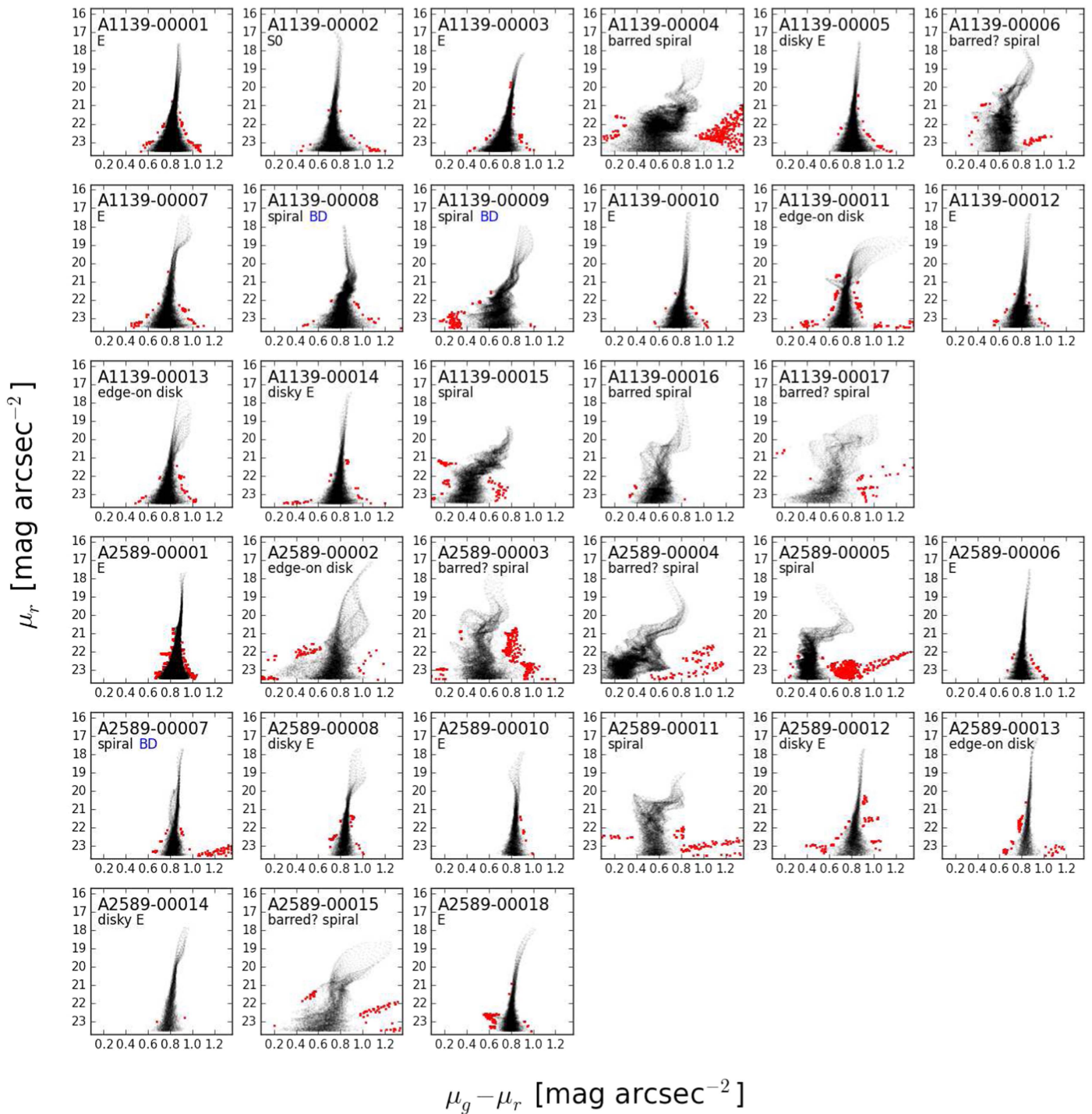


Figure 19. pCMDs after SE-detection-based masking and smoothing with the $0''.8$ -aperture spline kernel. Red dots show the pCMD outliers (see Section 3.1 for details).

2. Using the pCMDs after SE-detection-based masking, outlying pixels are determined using the method described in Section 3.1 (Figure 19). Some of the selected outliers may be substructures of target galaxies, but the possible over-masking does not significantly change the major trends of the pCMDs.
3. The pCMD outliers and their neighboring pixels within $0''.8$ distance (seeing size) are additionally masked, because those neighboring pixels may also be affected by the contaminants (Figure 20). This additional masking

is particularly important for late-type galaxies, which are poorly masked in the SE-detection-based method.

The final pCMDs after these processes are shown in Figure 7.

The full plots for the alternative procedure are also presented in Figures 21–23, and the final pCMDs are shown in Figure 8. Although the pCMDs resulting from the first-step masking in the two procedures are quite different from each other (Figures 19 and 22), the difference in the final pCMDs is smaller (Figures 7–9), owing to the secondary masking process based on the pCMD outliers.

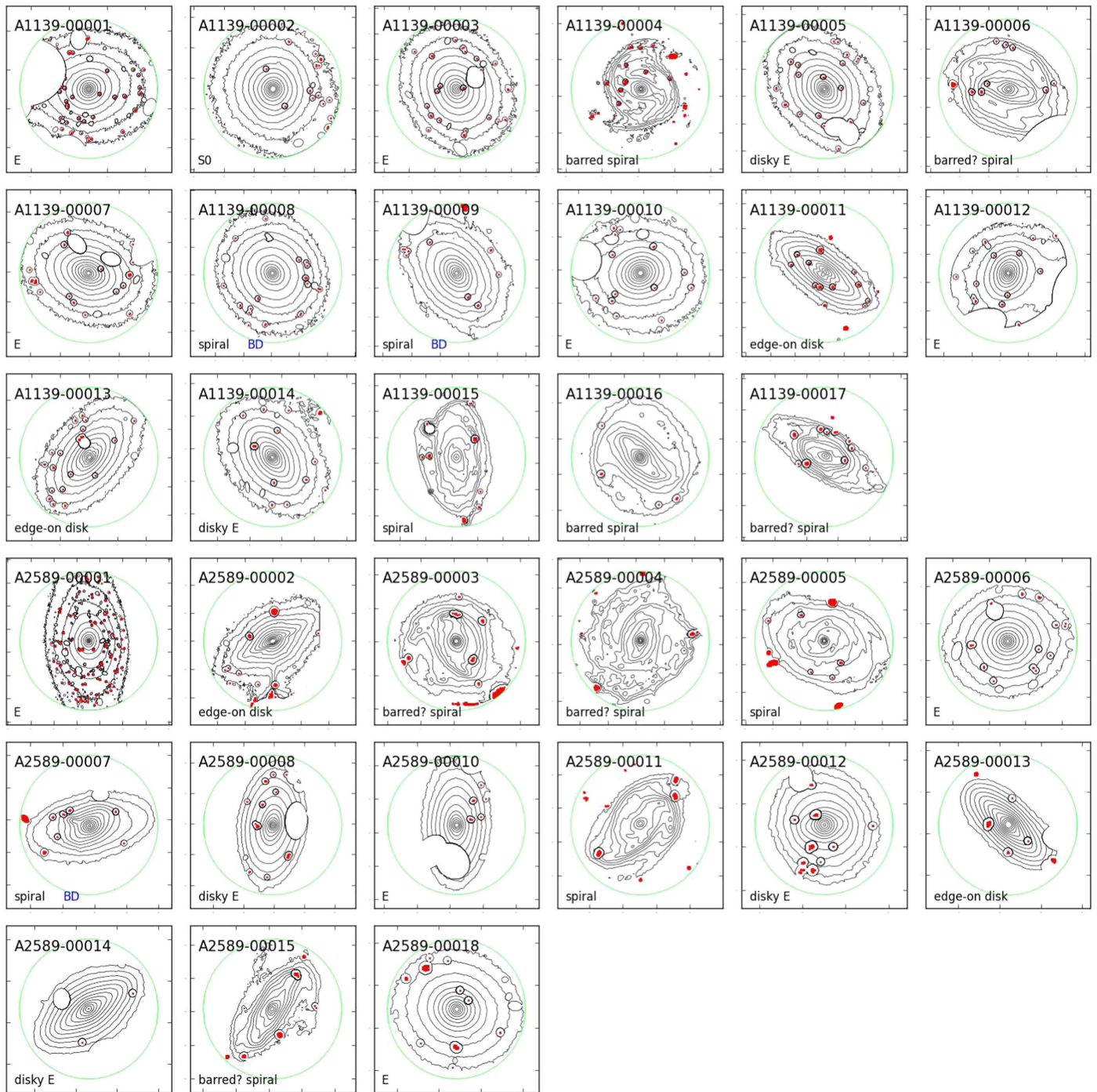


Figure 20. Surface brightness contour maps after masking pCMD outliers and their neighboring pixels within $0''.8$. The outlying pixels defined in Figure 19 are marked as red dots. The green circle indicates the spatial extent for the final pixel analysis of each target, which is defined at Step 2 of the alternative procedure in Section 3.2.

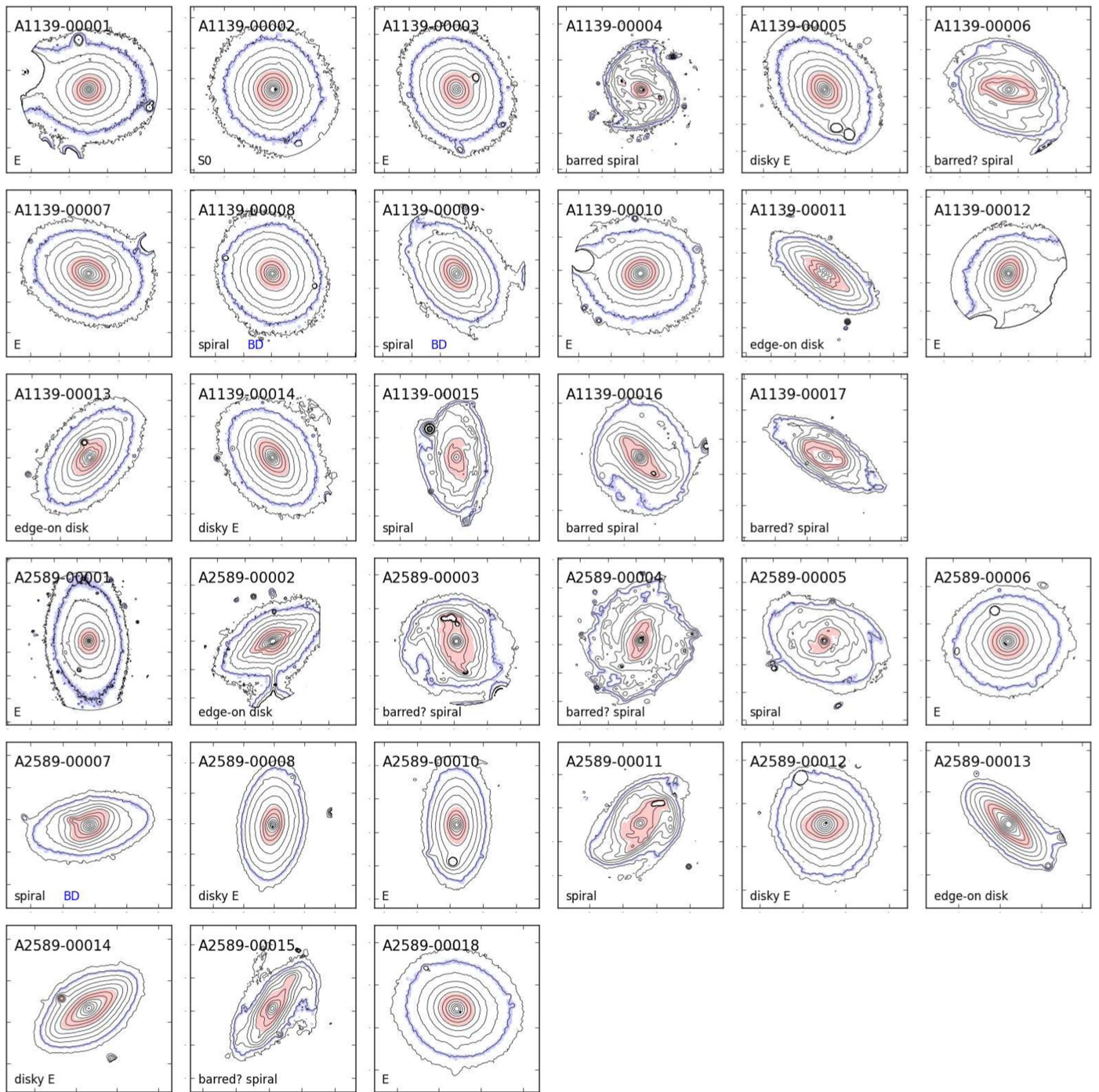


Figure 21. Surface brightness contour maps after $R(\mu_r)$ -based masking: the same as Figure 18, except that these are from the alternative masking procedure.

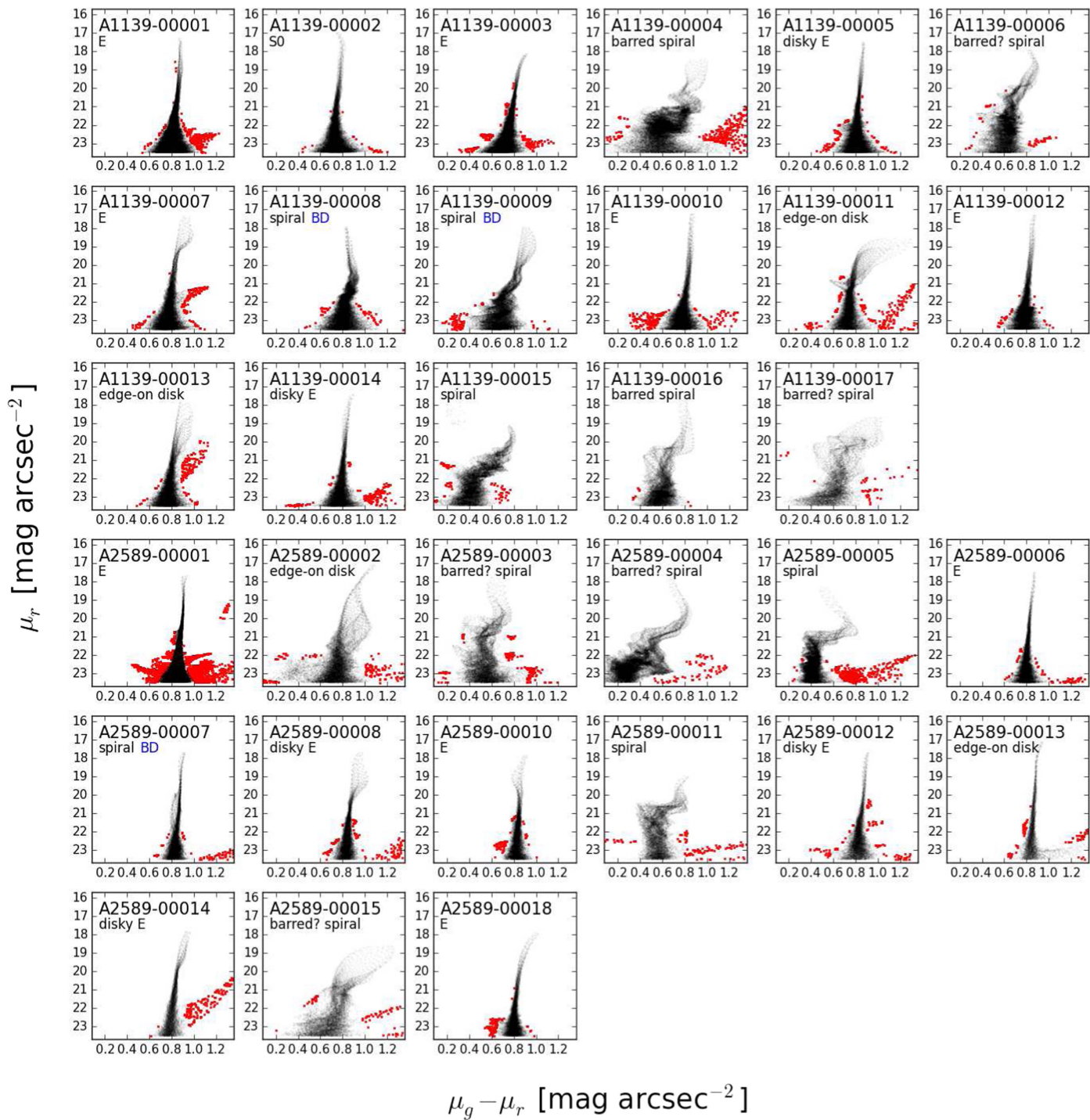


Figure 22. pCMDs after $R(\mu_r)$ -based masking and smoothing with the $0''.8$ -aperture spline kernel: the same as Figure 19, except that these are from the alternative masking procedure.

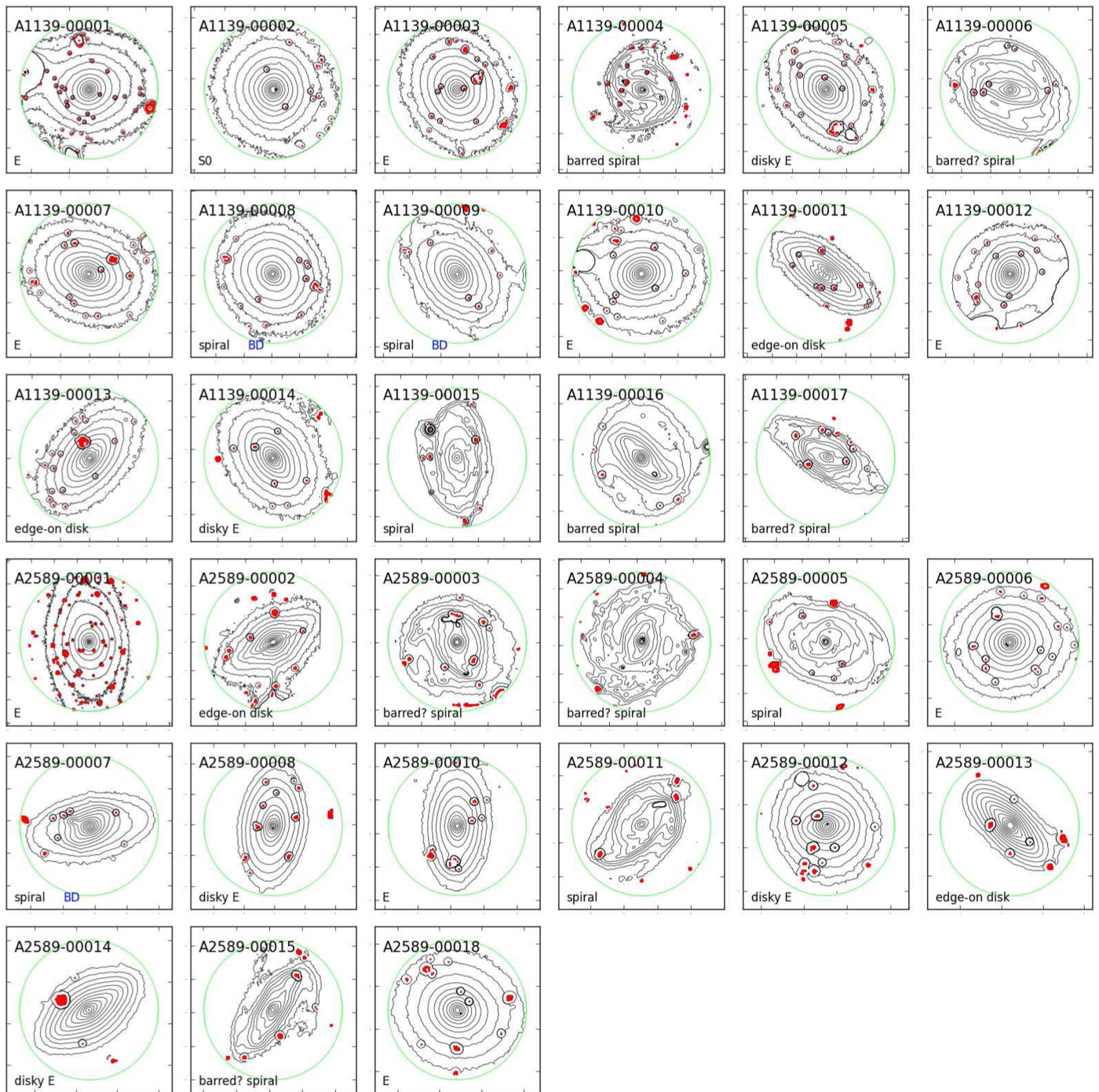


Figure 23. Surface brightness contour maps after masking the pCMD outliers and their neighboring pixels within $0''.8$: the same as Figure 20, except that these are from the alternative masking procedure.

Appendix B Results from the pCMDs after the Alternative Masking Procedure

All figures in Section 4 are based on the pCMDs after the standard masking procedure, and the results from the alternative procedure were omitted for better readability. The differences between the final results from the two different procedures are not significant. In this section, those omitted results are presented.

Figures 24–27 are the alternative procedure versions of Figures 10–12 and 16. The results from the alternative

procedure show little difference from the results from the standard procedure. Most sample galaxies show little change in their distributions on the plots, particularly for elliptical galaxies. Only a few spiral galaxies show considerable change in their pCMD parameters (e.g., A1139-00015 and A2589-00011), which result from incomplete masking of contaminants that occurs in spiral galaxies more readily. However, those changes do not affect our main conclusions at all. Table 5 lists the pCMD parameter values of the target galaxies from the alternative procedure, which are used in Figures 24–27.

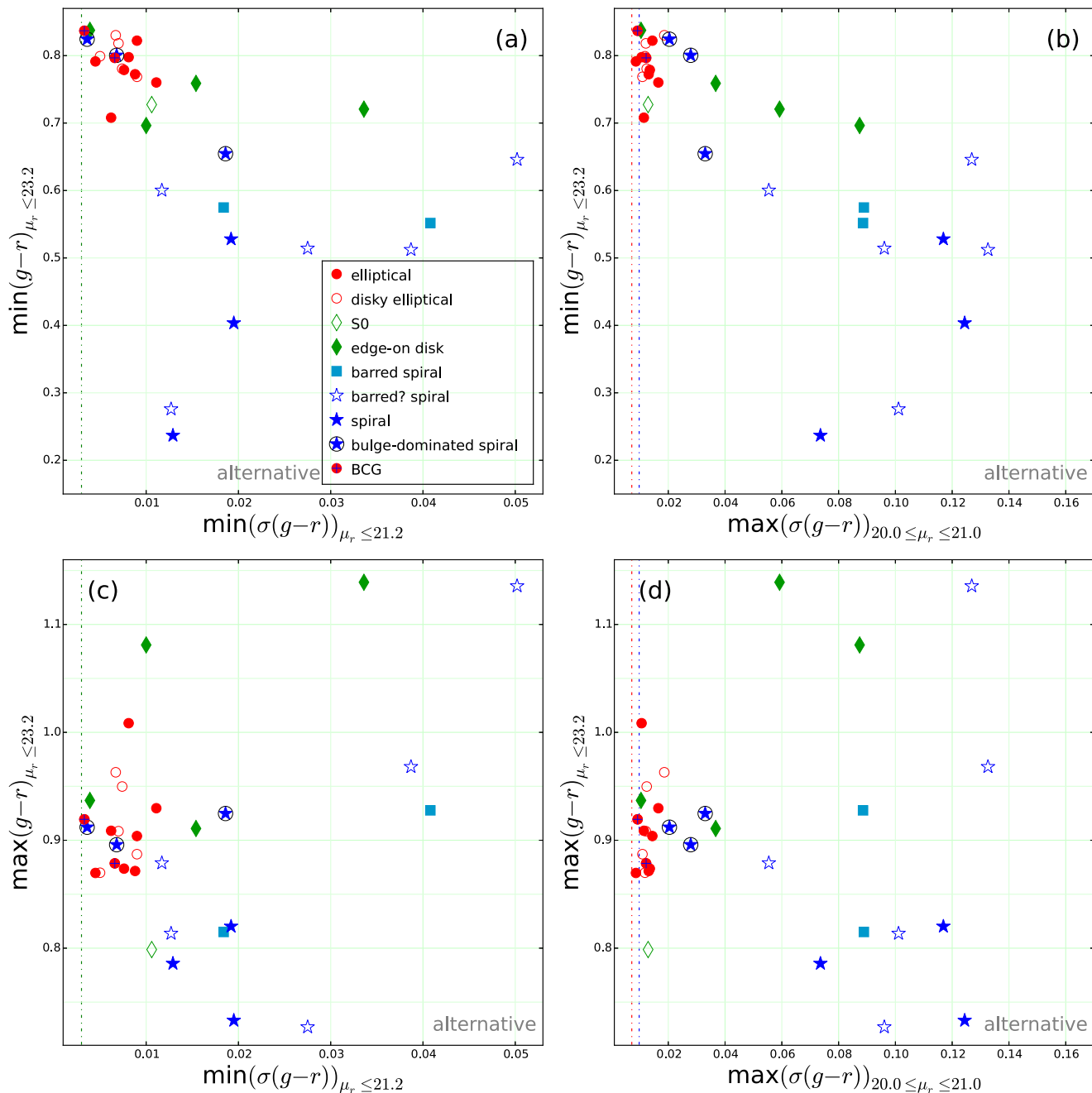


Figure 24. Correlations between pCMD parameters, based on the pCMDs after the alternative procedure: (a) the minimum $g-r$ color at $\mu_r \leq 23.2$ mag arcsec $^{-2}$ vs. the minimum $g-r$ color dispersion at $\mu_r \leq 21.2$ mag arcsec $^{-2}$, (b) the minimum $g-r$ color at $\mu_r \leq 23.2$ mag arcsec $^{-2}$ vs. the maximum $g-r$ color dispersion at $20.0 \leq \mu_r \leq 21.0$ mag arcsec $^{-2}$, (c) the maximum $g-r$ color at $\mu_r \leq 23.2$ mag arcsec $^{-2}$ vs. the minimum $g-r$ color dispersion at $\mu_r \leq 21.2$ mag arcsec $^{-2}$, and (d) the maximum $g-r$ color at $\mu_r \leq 23.2$ mag arcsec $^{-2}$ vs. the maximum $g-r$ color dispersion at $20.0 \leq \mu_r \leq 21.0$ mag arcsec $^{-2}$. The symbols are the same as those in Figure 10.

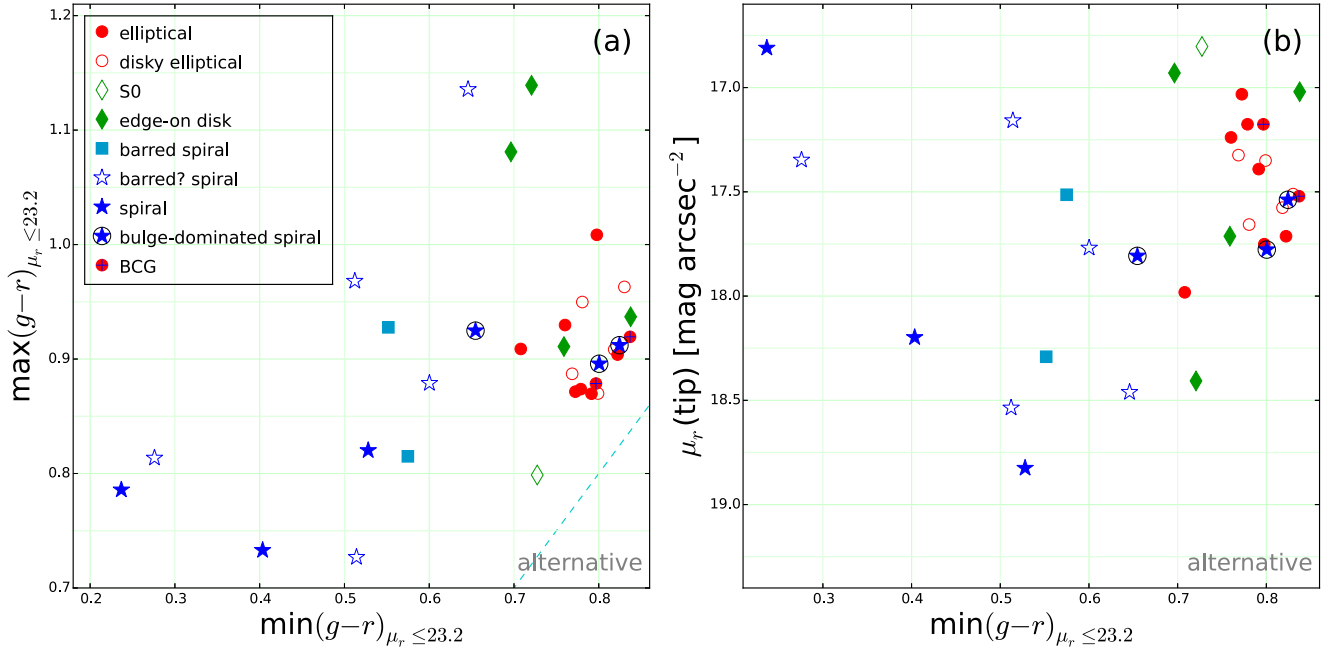


Figure 25. (a) The maximum vs. minimum values of mean $g - r$ color at $\mu_r \leq 23.2$ mag arcsec $^{-2}$, and (b) the brightest μ_r vs. the minimum $g - r$ color at $\mu_r \leq 23.2$ mag arcsec $^{-2}$, based on the pCMDs after the alternative masking procedure. The symbols are the same as those in Figure 11.

Table 5
pCMD Parameters from the Alternative Procedure

Name	$\min(g - r)$ $\mu_r \leq 23.2$	$\max(g - r)$ $\mu_r \leq 23.2$	$\mu_r(\text{tip})$	$\min(\sigma(g - r))$ $\mu_r \leq 21.2$	$\max(\sigma(g - r))$ $20.0 \leq \mu_r \leq 21.0$	$\max(\sigma(g - r))$ $18.5 \leq \mu_r \leq 19.5$	$\max(\sigma(g - r))$ $\mu_r \leq 21.2$
A1139-00001	0.797	0.879	17.18	0.007	0.012	0.014	0.014
A1139-00002	0.727	0.799	16.80	0.011	0.013	0.013	0.017
A1139-00003	0.708	0.909	17.98	0.006	0.011	0.012	0.016
A1139-00004	0.552	0.928	18.29	0.041	0.089	0.071	0.103
A1139-00005	0.799	0.870	17.35	0.005	0.012	0.012	0.012
A1139-00006	0.600	0.879	17.77	0.012	0.055	0.037	0.055
A1139-00007	0.760	0.930	17.24	0.011	0.017	0.048	0.049
A1139-00008	0.800	0.896	17.78	0.007	0.028	0.017	0.028
A1139-00009	0.655	0.925	17.81	0.019	0.033	0.049	0.049
A1139-00010	0.772	0.872	17.03	0.009	0.013	0.014	0.014
A1139-00011	0.721	1.139	18.41	0.034	0.059	0.136	0.136
A1139-00012	0.779	0.874	17.18	0.008	0.013	0.015	0.015
A1139-00013	0.759	0.911	17.71	0.015	0.037	0.052	0.052
A1139-00014	0.769	0.887	17.32	0.009	0.011	0.017	0.017
A1139-00015	0.237	0.786	16.81	0.013	0.074	0.245	0.245
A1139-00016	0.575	0.815	17.51	0.018	0.089	0.033	0.089
A1139-00017	0.512	0.968	18.54	0.039	0.133	0.116	0.136
A2589-00001	0.837	0.919	17.52	0.003	0.009	0.005	0.016
A2589-00002	0.696	1.081	16.93	0.010	0.087	0.070	0.087
A2589-00003	0.514	0.727	17.16	0.028	0.096	0.055	0.096
A2589-00004	0.276	0.814	17.35	0.013	0.101	0.032	0.101
A2589-00005	0.404	0.733	18.20	0.019	0.124	0.044	0.124
A2589-00006	0.791	0.870	17.39	0.004	0.009	0.009	0.009
A2589-00007	0.824	0.912	17.54	0.004	0.020	0.010	0.020
A2589-00008	0.830	0.963	17.51	0.007	0.019	0.048	0.048
A2589-00010	0.822	0.904	17.71	0.009	0.014	0.032	0.032
A2589-00011	0.528	0.820	18.82	0.019	0.117	0.029	0.117
A2589-00012	0.818	0.908	17.58	0.007	0.012	0.010	0.015
A2589-00013	0.838	0.937	17.02	0.004	0.010	0.006	0.011
A2589-00014	0.781	0.950	17.66	0.007	0.012	0.023	0.023
A2589-00015	0.646	1.136	18.46	0.050	0.127	0.157	0.157
A2589-00018	0.798	1.008	17.75	0.008	0.011	0.022	0.023

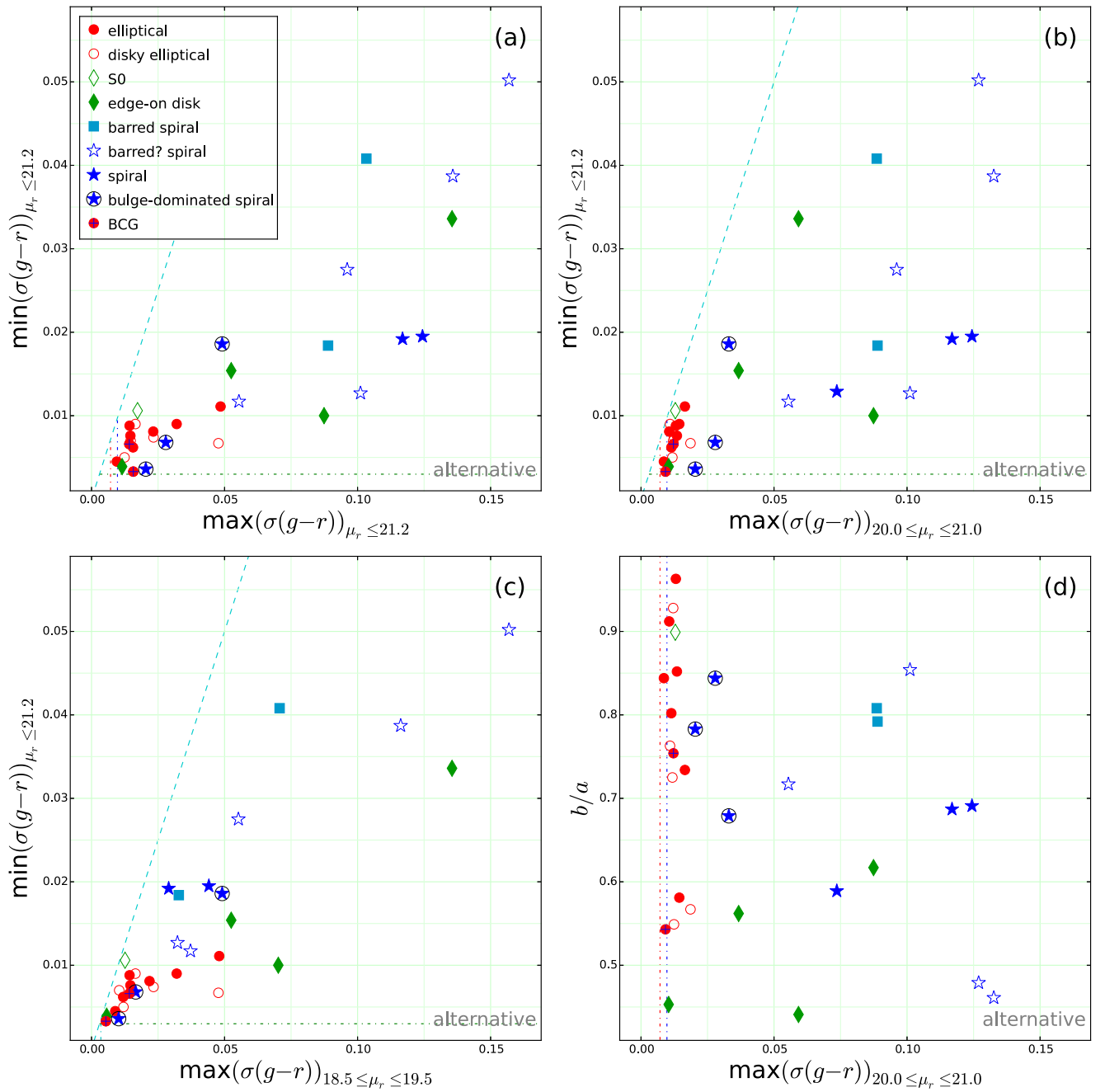


Figure 26. The minimum $g - r$ color dispersion at $\mu_r \leq 21.2$ mag arcsec $^{-2}$ vs. the maximum $g - r$ color dispersion at (a) $\mu_r \leq 21.2$ mag arcsec $^{-2}$, (b) $20.0 \leq \mu_r \leq 21.0$ mag arcsec $^{-2}$, and (c) $18.5 \leq \mu_r \leq 19.5$ mag arcsec $^{-2}$. (d) Axis ratio vs. the maximum $g - r$ color dispersion at $20.0 \leq \mu_r \leq 21.0$ mag arcsec $^{-2}$. These plots are the same as those in Figure 12, except that these are from the alternative masking procedure.

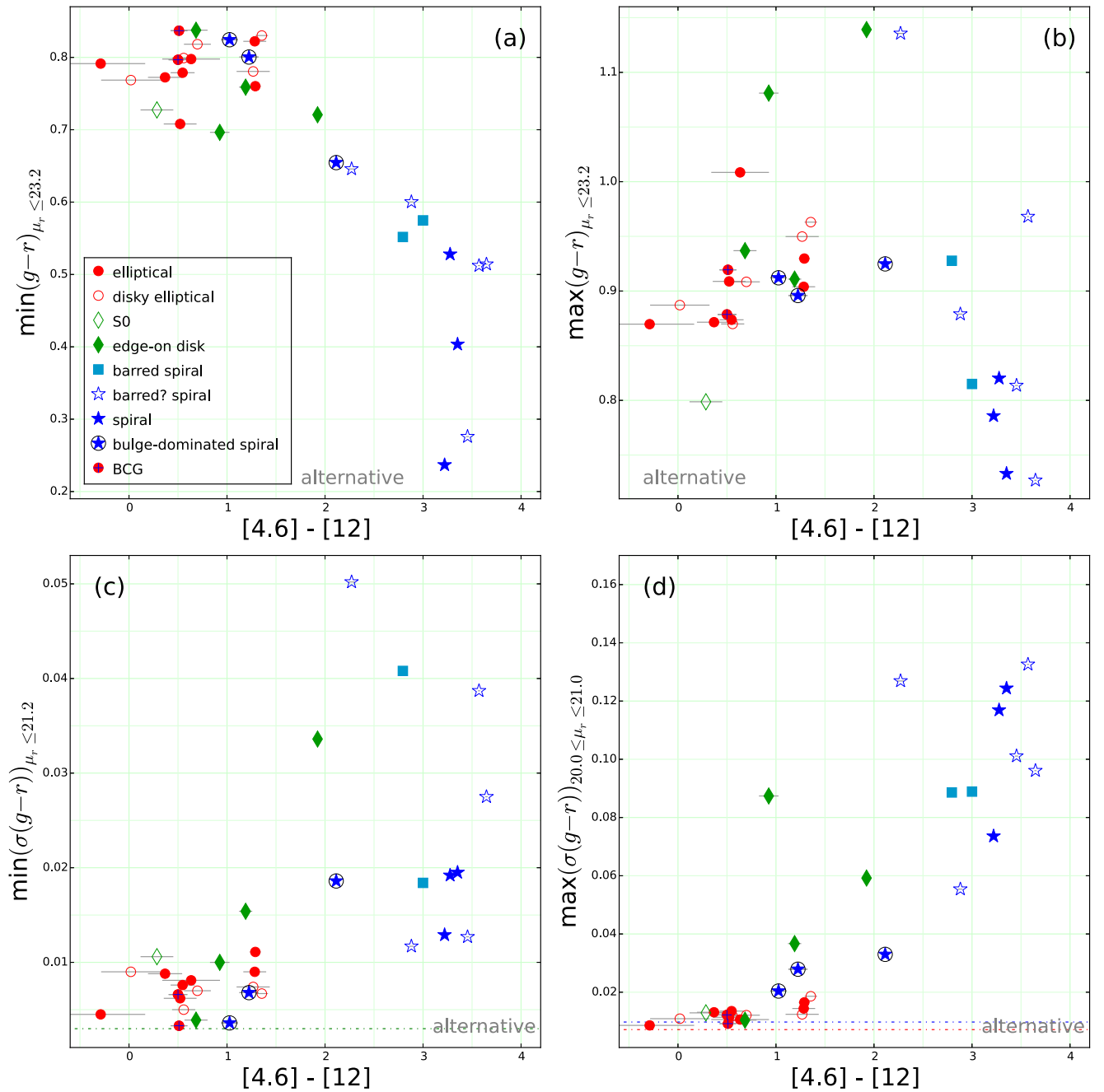


Figure 27. pCMD parameters vs. the *WISE* [4.6]–[12] color, based on the pCMDs after the alternative masking procedure: (a) the minimum $g - r$ color at $\mu_r \leq 23.2$ mag arcsec $^{-2}$, (b) the maximum $g - r$ color at $\mu_r \leq 23.2$ mag arcsec $^{-2}$, (c) the minimum value of $g - r$ color dispersion at $\mu_r \leq 21.2$ mag arcsec $^{-2}$, and (d) the maximum value of $g - r$ color dispersion at $20.0 \leq \mu_r \leq 21.0$ mag arcsec $^{-2}$. The dotted–dashed lines are the reliability limits as described in Figure 10.

ORCID iDs

Joon Hyeop Lee <https://orcid.org/0000-0003-3451-0925>

Hye-Ran Lee <https://orcid.org/0000-0002-1827-5454>

References

- Abraham, R. G., Ellis, R. S., Fabian, A. C., Tanvir, N. R., & Glazebrook, K. 1999, *MNRAS*, 303, 641
- Assef, R. J., Kochanek, C. S., Brodwin, M., et al. 2010, *ApJ*, 713, 970
- Bernardi, M., Roche, N., Shankar, F., & Sheth, R. K. 2011, *MNRAS*, 412, L6
- Bertin, E., & Arnouts, S. 1996, *A&AS*, 117, 393
- Bothun, G. D. 1986, *AJ*, 91, 507
- Conroy, C., & van Dokkum, P. G. 2016, *ApJ*, 827, 9
- de Grijs, R., Lee, J. T., Mora Herrera, M. C., Fritze-v. Alvensleben, U., & Anders, P. 2003, *NewA*, 8, 155
- Dressler, A. 1987, *ApJ*, 317, 1
- Fernández-Ontiveros, J. A., López-Sanjuan, C., Montes, M., Prieto, M. A., & Acosta-Pulido, J. A. 2011, *MNRAS*, 411, L21
- Fisher, D. B., & Drory, N. 2008, *AJ*, 136, 773
- Gadotti, D. A. 2009, *MNRAS*, 393, 1531
- George, K. 2017, *A&A*, 598, 45
- Ivezic, Z., Axelrod, T., Brandt, W. N., et al. 2008, *SerAJ*, 176, 1
- Jarrett, T. H., Cluver, M. E., Magoulas, C., et al. 2017, *ApJ*, 836, 182
- Jarrett, T. H., Cohen, M., Masci, F., et al. 2011, *ApJ*, 735, 112
- Kaviraj, S., Peirani, S., Khochfar, S., Silk, J., & Kay, S. 2009, *MNRAS*, 394, 1713
- Kim, K., Oh, S., Jeong, H., et al. 2016, *ApJS*, 225, 6
- Ko, J., Chung, H., Hwang, H. S., & Lee, J. C. 2016, *ApJ*, 820, 132

- Kormendy, J., Fisher, D. B., Cornell, M. E., & Bender, R. 2009, *ApJS*, **182**, 216
- Lanyon-Foster, M. M., Conselice, C. J., & Merrifield, M. R. 2007, *MNRAS*, **380**, 571
- Larson, R. B. 1974, *MNRAS*, **166**, 585
- Lee, J., & Yi, S. K. 2013, *ApJ*, **766**, 38
- Lee, J. H., Kim, M., Ree, C. H., et al. 2013, *ApJL*, **762**, L4
- Lee, J. H., Kim, S. C., Park, H. S., et al. 2011, *ApJ*, **740**, 42
- Lee, J. H., Kim, S. C., Ree, C. H., et al. 2012, *ApJ*, **754**, 80
- Lee, J. H., Lee, M. G., & Hwang, H. S. 2006, *ApJ*, **650**, 148
- Lee, J. H., Lee, M. G., Park, C., & Choi, Y.-Y. 2008, *MNRAS*, **389**, 1791
- Lee, J. H., Oh, S., Jeong, H., et al. 2017, *ApJ*, **844**, 81
- Liu, F. S., Jiang, D., Gui, Y., et al. 2016, *ApJL*, **822**, L25
- Naab, T., Khochfar, S., & Burkert, A. 2006, *ApJL*, **636**, L81
- Oh, S., Kim, K., Lee, J. H., et al. 2018, *ApJS*, submitted
- Oser, L., Ostriker, J. P., Naab, T., Johansson, P. H., & Burkert, A. 2010, *ApJ*, **725**, 2312
- Park, C., & Hwang, H. 2009, *ApJ*, **699**, 1595
- Pastrello, N., Forbes, D. A., Usher, C., et al. 2015, *MNRAS*, **451**, 2625
- Patridge, R. R., & Peebles, P. J. E. 1967, *ApJ*, **147**, 868
- Peng, C. Y., Ho, L. C., Impey, C. D., & Rix, H.-W. 2002, *AJ*, **124**, 266
- Peng, C. Y., Ho, L. C., Impey, C. D., & Rix, H.-W. 2010, *AJ*, **139**, 2097
- Schlafly, E. F., & Finkbeiner, D. P. 2011, *ApJ*, **737**, 103
- Searle, L., & Zinn, R. 1978, *ApJ*, **225**, 357
- Sheen, Y.-K., Smith, R., Jaffé, Y., et al. 2017, *ApJL*, **840**, L7
- Sheen, Y.-K., Yi, S. K., Ree, C. H., et al. 2016, *ApJ*, **827**, 32
- Skrutskie, M. F., Cutri, R. M., Stiening, R., et al. 2006, *AJ*, **131**, 1163
- Tinsley, B. M. 1972, *ApJ*, **178**, 319
- Tojeiro, R., Masters, K. L., Richards, J., et al. 2013, *MNRAS*, **432**, 359
- Toomre, A. 1977, in *The Evolution of Galaxies and Galaxy Populations*, ed. B. M. Tinsley & R. B. Larsen (New Haven, CT: Yale Univ. Obs), 401
- van Dokkum, P. G., Whitaker, K. E., Brammer, G., et al. 2010, *ApJ*, **709**, 1018
- Wright, E. L., Eisenhardt, P. R. M., Mainzer, A. K., et al. 2010, *AJ*, **140**, 1868
- York, D. G., Adelman, J., Anderson, J. E., Jr., et al. 2000, *AJ*, **120**, 1579